

ANALYZING PATTERNS IN SUBSEASONAL TO SEASONAL VARIABILITY OF WIND  
DROUGHT IN MIDLATITUDE NORTH AMERICA

A Thesis

Presented to the Faculty of the Graduate School

of Cornell University

In Partial Fulfillment of the Requirements for the Degree of

Master of Science

by

Blake Harrison Johannes Himes

August 2022

© 2022 Blake Harrison Johannes Himes

## ABSTRACT

Renewably sourced electricity generation capacity in the United States is accelerating, resulting in a power supply that is increasingly linked to the weather and climate patterns that govern renewable resources. Wind Drought (WD) is a highly variable field throughout time and space with important implications for wind energy generation. Monthly and seasonal patterns in WD were identified and correlations with proposed influences of low wind speeds revealed factors that enhanced or suppressed WD conditions. On a synoptic scale, WD shares a correlation pattern with the seasonal undulations in the jet stream and its routing of midlatitude cyclones. For certain months and locations, WD is correlated with fluctuations in the ENSO, NAO, and PNA indices. Composites of positive and negative modes identified connections with WD anomalies consistent with the typical impacts of each climate mode on large-scale flow patterns and weather effects.

## BIOGRAPHICAL SKETCH

Blake Himes received his master's degree in Atmospheric Science from Cornell University as the inaugural student in the Department of Earth and Atmospheric Sciences' five-year combined B.S./M.S. program. He graduated from the College of Agriculture and Life Sciences at Cornell University in May 2021 with a Bachelor of Science in Atmospheric Science. As a research assistant with the Emergent Climate Risk Laboratory under the direction of Dr. Toby R. Ault, Blake worked to develop a curriculum targeted at high school students called EduWRF. This endeavor enabled students to engage with numerical weather prediction (NWP) at a young age through running the Weather Research and Forecasting (WRF) dynamical model in the cloud and providing a package of scripts to visualize its output. While at Cornell, Blake was a double bassist in the Cornell Symphony Orchestra and an *a cappella* musician with The Chordials. He enjoyed opportunities to perform frequently and tour with both groups, most notably travelling with CSO to Taipei in 2019 to play Mahler's "Titan" Symphony No. 1 and Mendelssohn's Violin Concerto in E Minor alongside the Taiwan Symphony Orchestra. He was also a leader within the Pi chapter of the Delta Phi fraternity, known on campus as Llenroc. In the fall, Blake will begin a job at Ramboll US in Novato, California as an Air Quality Consultant. During his free time, Blake enjoys making and listening to music, travelling, tossing a frisbee, sailing, gazing at clouds, and hanging out with close friends and family.

*I would like to dedicate this thesis to my parents, Annette and Brett Himes, for their unwavering support through all of my academic endeavors.*

## ACKNOWLEDGMENTS

I am grateful to many mentors, colleagues, and friends whose constant support and companionship helped make my completion of my master's degree and thesis a reality. First and foremost, I would like to acknowledge my graduate thesis committee chair and undergraduate academic advisor, Dr. Toby R. Ault, who provided the direct inspiration for me to pursue graduate studies in Atmospheric Science and assisted me in incalculably many ways during my time at Cornell. Without his wisdom and enthusiastic approach to education, my experience at Cornell could not have been as fulfilling. I am thankful for the many other faculty members who took care to help me further my academic pursuits, especially Drs. Natalie Mahowald, Max Zhang, Mark Wysocki, Arthur DeGaetano, and Peter Hitchcock. I greatly appreciate the community connected to the Emergent Climate Risk Lab at Cornell for their assistance in data collection and computer programming, including Jiajun Gu, Dr. Jeff Sward, Dr. Dimitris Herrera, Bo Yuan, Marty Sullivan, Marc Alessi, and Rick Moore. I am thankful for my classmate Tavyen Matthews and his unconditional encouragement and friendship throughout my experience at Cornell. I also find it important to acknowledge my friends and housemates that made my experience in Ithaca a truly memorable one. Finally, I must thank my mother Annette, father Brett, and sister Audrey for always having my back and helping me navigate the many challenges of life as a young adult and helping me grow immeasurably along the way.

## TABLE OF CONTENTS

<b>1. INTRODUCTION</b> .....	<b>1</b>
1.1 THE NEED TO UNDERSTAND WIND DROUGHT FOR SUSTAINABLE ENERGY PRODUCTION.....	1
1.2 INSIGHTS FROM RECENT RESEARCH INTO WIND DROUGHT AND NEED FOR FURTHER STUDY .....	2
<b>2. DATA &amp; METHODS</b> .....	<b>3</b>
2.1 REANALYSIS DATA SOURCE AND WIND DROUGHT VARIABLE DEFINITION.....	3
2.2 CLIMATE INDEX DATA AND COMPOSITE ANALYSIS.....	6
<b>3. RESULTS</b> .....	<b>6</b>
3.1 ANALYSIS OF WIND DROUGHT SPATIAL AND TEMPORAL VARIABILITY .....	6
3.2 SELECTION OF EXTREME HISTORICAL WD EVENTS .....	9
3.3 PRINCIPAL COMPONENT ANALYSIS OF WIND DROUGHT .....	10
3.3.1 Examining PC Correlation Patterns with WD Anomalies and $Z_{250}$ Anomalies .....	11
3.3.2 Examining Correlations Between Teleconnection Patterns and WD Anomalies.....	14
3.4 ANALYSIS OF COMPOSITE WD ANOMALIES UNDER MODERATE TO STRONG TELECONNECTION MODES .....	15
<b>4. DISCUSSION</b> .....	<b>17</b>
4.1 INTERPRETATION OF RESULTS FROM PCA AND CORRELATION ANALYSIS .....	17
4.2 PROPOSED CONTRIBUTIONS FROM CLIMATE MODES ON WD PREVALENCE.....	20
4.3 INSPECTION OF WD ANOMALIES DURING MONTHS WITH EXTREMELY HIGH WD .....	22
<b>5. CONCLUSION</b> .....	<b>26</b>
<b>6. FIGURES</b> .....	<b>28</b>
<b>7. REFERENCES</b> .....	<b>47</b>

## 1. INTRODUCTION

### 1.1 The Need to Understand Wind Drought for Sustainable Energy Production

The crisis-level threats to human civilization posed by the impacts of climate change have spurred great dialogue and action to mitigate emissions of carbon dioxide (CO<sub>2</sub>) and other greenhouse gases emitted as byproducts of anthropogenic activities. In the United States and many other nations, the energy sector is the greatest contributor to emissions, primarily from combustion of fossil fuels such as coal, petroleum, and natural gas. Global energy-related annual CO<sub>2</sub> emissions have averaged 32.8 gigatons (Gt) of CO<sub>2</sub> since 2017, though emissions from advanced economies such as the United States have fallen by 1.8 Gt CO<sub>2</sub> since the turn of the century (IEA, 2022). Many nations recognize the importance of mounting a swift transition toward resilient energy systems that use renewable, clean sources to generate electricity. Indeed, new wind turbine installations, particularly offshore, are accelerating the United States' expansion of renewable energy generation capacity. While global electricity demand is projected to grow by 2.7% year-over-year through 2024, renewables are expected to expand by 8% and will cover over 90% of growth in net demand for the same period (IEA, 2022).

Clean energy sources including wind, solar, and hydroelectric are expected to comprise one third of domestic electricity generation by 2026, up from 19.25% in 2021 (Wamstead et al., 2022). As a result, energy generation capacity becomes increasingly linked to the weather and climate patterns, leaving power grids susceptible to production shortages when available resources are insufficient to meet demand. Sufficient long-distance electricity transmission systems could help to compensate for interregional discrepancies in resource availability, but this counteractive effect is constrained in the U.S. by lacking infrastructure and bottlenecks in long-range transmission. (Pryor et al., 2018). On short time horizons, grid-scale battery storage serves

to mitigate variability inherent to renewable energy and maximize the electricity's value. In addition to providing operating reserves for the power plant, batteries perform arbitrage via load-leveling – using periods of excess generation such as a windy night to charge while discharging during high-cost peak hours – and reduced curtailment of generation in periods of asymmetric supply and demand (Bowen et al., 2019). Battery storage is critical to reliably expanding the capacity for generation and delivery of electricity derived from renewable resources but does not eliminate the susceptibility of the renewable installations to the chaotic whims of the atmosphere. This rapidly increasing share of power derived from renewables can be viewed as a double-edged sword, as benefits from decreased carbon emissions can be limited by prolonged or severe resource deficits and shortages in electricity supply due to atmospheric conditions.

## 1.2 Insights from Recent Research into Wind Drought and Need for Further Study

This study into the leading patterns and modes of variability of Wind Drought (WD) and correlations with other weather variables and climate indices is built on several prior studies into resource drought (RD). Gu et al. (2022) analyzed occurrence, persistence, and return period of solar and wind resource drought (S+W RD) over land within the contiguous United States (CONUS) and found that occurrence and persistence are driven by wind RD on a geographical basis and by solar RD on a temporal basis. Pryor et al. (2018) utilized the Weather Research & Forecasting (WRF) model to calculate expected annual energy production across the eastern United States and found that wind speed variability manifests on different timescales, driven by the frequency and tracking of midlatitude cyclones for seasonal to interannual scales. Further, their study found that climate modes such as ENSO, NAO, and PNA (El Niño Southern Oscillation, North Atlantic Oscillation, and Pacific/North American pattern, respectively) are important influences on wind regimes and extremes in energy production on a regional scale

(Pryor et al., 2018). Since WD is an extrapolated variable, it is useful to have indicators that are correlated with certain measured indices or otherwise known and forecastable variables.

Examining spatial variability in WD patterns throughout the months and seasons of the year to find correlations to dominant weather regimes and sources of intra-annual climate variability enables attempts to diagnose contributing factors to WD and inform predictions of locally available wind energy on the subseasonal to seasonal scale. Month-specific correlations between climate modes and synoptic to continental scale weather patterns provide useful information on spatiotemporal connections between key weather and climate indicators that can be used to anticipate episodes of enhanced WD and improve location-specific forecasts.

The objectives of the following research are to:

1. Examine months with anomalously high WD to draw conclusions based on the spatial WD distribution and dominant weather regimes that contributed to the extreme WD.
2. Identify patterns in the spatial variability of WD across its annual cycle using Principal Component Analysis
3. Assess correlation between leading WD variability patterns and primary drivers of large-scale flow (the jet stream) and local climate variability (ENSO, NAO, PNA)

## 2. DATA & METHODS

### 2.1 Reanalysis Data Source and Wind Drought Variable Definition

The Modern-Era Retrospective Analysis for Research and Application, version 2 (MERRA-2) is NASA's current dynamical climate reanalysis model, with state-of-the-art data assimilation from *in situ* and satellite measurements (Gelaro et al., 2017). The two-dimensional, one-hourly averaged U and V wind components at 50 meters from MERRA-2 were downloaded

from the Goddard Earth Sciences Data and Information Services Center (GES DISC) website for the time period 01-01-1980 through 12-31-2021 (GMAO 2015). Likewise, the instantaneous three-dimensional monthly mean geopotential height in meters at 250 hPa from MERRA-2 was downloaded (GMAO 2015). The chosen spatial domain is a rectangular grid from 67W to 124.375W and 24.5N to 49N, which spans CONUS and most regions of interest offshore of the United States. MERRA-2 has 0.5 degrees latitude by 0.625 degrees longitude gridded spatial resolution.

The Wind Drought (WD) variable was set as the total number of days per month where the average daily wind speed,  $\bar{U}_{daily} = \frac{\sum \sqrt{\|u^2\| + \|v^2\|}}{24}$ , was less than 3 meters per second.

Mathematically:

$$WD_{i,j,t} = \#(\bar{U}_{daily} < 3),$$

where  $WD_{i,j,t}$  represents the value for WD during month  $t$  at the  $i^{\text{th}}$  grid point from the western domain boundary and the  $j^{\text{th}}$  grid point from the southern boundary. The value for WD, with units of days per month, was calculated for each grid point in the domain for 42 years (504 months) from January 1980 through December 2021. The threshold of 3 meters per second was chosen to represent a daily average wind speed where significant portions of the day would be minimally suitable for wind energy production, which generally tapers off at speeds below 4.0 m/s (Yu et al., 2009). Other studies have chosen thresholds of 3.5 m/s at 80 m (extrapolated via power law to 3.3 m/s at 50 m) and 4 m/s at 100 m, respectively, rendering this threshold for WD more constricting than prior studies – cf. wind RD and “calms” (Gu et al., 2022; Pryor et al., 2018). A light breeze below 3 m/s is enough to feel on one’s face and rustle leaves but does not transfer enough momentum to the large industrial wind turbines to sustain electricity generation,

and prolonged calm periods can leave blade rotation and energy production at a standstill. The spatially averaged WD fraction over the entire domain was calculated and plotted vs. time to reveal both the annual cycle of WD occurrence and identify extreme positive outliers in spatially averaged WD fraction. Six Augusts – 1983, 1984, 1990, 1996, 2005, and 2014 – were identified as having the WD fractions over 0.20 for the month. The WD anomalies, calculated by removing the monthly mean from the WD values for each individual month, were plotted and examined to characterize the strength and extent of this WD event. WD anomalies for each month and season were calculated by removing the long-term mean from the monthly and seasonal WD mean. Further WD anomalies for climate composites and outlier WD months subtract the mean WD across all Januaries, Februaries, etc. from the WD values for corresponding individual months or groups of months to remove annual trends from the WD data.

WD data was prepared for PCA by scaling the data to remove the mean and normalize to unit variance. Data for each location was grouped by month/season and reduced along the time dimension, using 42 observations per location. PCA was conducted for  $n = 10$  components to identify independent, uncorrelated patterns within the data, expressed as dipole patterns in the resulting spatial loadings. A target of 80% explained variance was set to capture most of the variability and simplify analysis. The first two PCs were retained for each month and season, explaining between 75% and 81% of all WD variance across all months and seasons. Singular Value Decomposition (SVD) was used to generate a time series for each PC, enabling correlation analysis between WD PCs and the scaled WD anomalies as well as 250 hPa geopotential height ( $Z_{250}$ ) anomalies. The inverses of the PC time series were used in correlation analysis to have negative correlations correspond to enhanced WD.

## 2.2 Climate Index Data and Composite Analysis

Monthly ERSSTv5 sea surface temperature (SST) anomalies for the Niño 3.4 region (5N-5S, 170W-120W) using a 1991-2020 base period were downloaded from the Monthly Atmospheric and SST Indices page of the Climate Prediction Center website (CPC, 2022). Monthly time series for the NAO and PNA indices were downloaded from the Climate Prediction Center's monthly tabulated NAO and PNA historical index dating back to 1950 using a 1981-2010 base period. Scaled WD anomalies were correlated with the time series of ENSO, NAO, and PNA and plotted by month. Composite WD anomalies for each month that experienced a moderate to strong positive or negative climate mode, defined as any month where the index was above 1 or below -1, were examined for common spatial patterns of enhanced/suppressed WD. Composites were analyzed in conjunction with the previous correlations to draw conclusions about the interannual variability of WD in relation to climate modes and their associated weather regimes.

## 3. RESULTS

### 3.1 Analysis of Wind Drought Spatial and Temporal Variability

The variable of interest for Principal Component Analysis was selected as wind drought days per month, computed for each location as the number of days in each month where the average daily wind speed at 50 meters above ground level (AGL) was below a threshold of 3 m/s. The hourly wind velocity data from MERRA-2 in U and V components was simplified into a scalar daily average wind speed value. The total number of WD days in each month was then saved for all 4,600 grid points and 504 months of the study domain. Removing the directional attribute of the data and lowering the temporal resolution as such confines the application of these findings to quasi-continuously operating systems that are independent of direction. Wind

energy turbines, including many industrial and residential products, are designed to be able to harness wind energy from any direction – either through a yaw system and motor that orients the nacelle and blades into the wind or through designs that function omnidirectionally (Wind Energy Technologies Office). Given this, the findings that follow from analyzing this derived variable have direct application to understanding the susceptibility of a particular location to WD conditions specific to each month and season throughout the calendar year.

To offer a sense of the climatological distribution of wind throughout the spatial domain, the long term mean wind speed was plotted in Figure 1. The most prominent feature that emerges is the broad swath of the United States interior that exhibits a mean wind speed at 50 m AGL exceeding 7 m/s, or over 15 mph, spanning the lower and upper Great Plains and the upper Midwest. Regions with blue and blue-green shading have lower average wind speeds, which appear associated with more complex and rough terrain and topography, such as mountains, forests, or both. These types of terrain exhibit large roughness lengths, conventionally expressed as  $Z_0$  with units in meters, which increases drag on the more turbulent flow and enhances the rate of momentum transfer to the surface (Stull 1988). Contrastingly, locations with small roughness lengths ( $Z_0 \ll 1$ ) such as the flat, prairied U.S. interior and the open sea experience less friction and have a significantly smaller drag effect on the wind speed. At more than twice the threshold value of 3 m/s, one might suppose that windier regions are generally less susceptible to the relatively rare occurrence of WD conditions than are areas in the terrestrial contiguous United States with lighter average winds. This reasoning arises from the assumption that with higher mean wind speeds, a specific location's distribution of daily wind speeds will tend to have fewer instances below 3 m/s. However, the variance across time differs between grid point locations, so

conclusions about the frequency and extent of wind drought events cannot be drawn directly from the long-term mean wind speed.

Monthly and seasonal climatologies for WD days per month are shown in Figures 2 - 3, with corresponding WD anomalies in Figures 4 - 5. In the climatology plots, green shading throughout the Great Plains and upper Midwest (indicating a very low average of WD days) persists across the monthly and seasonal averages, providing evidence for the decreased susceptibility to WD conditions in windier climates. The Cascade Range in the Pacific Northwest and mountainous regions of Idaho and northern California experience frequent bouts of WD that appear yellow and red in the climatology plots, concentrated most heavily in the summer months. Signals for severe WD (shaded orange and red) in coastal southern California are elevated in the summer and fall, while WD conditions for the California's central valley show maximum extent in the winter months. WD persistence for the Sierra Madre Occidental range in Mexico exceeds twenty days per month in the summer months and exhibits a regular annual WD cycle, with maximum spatial and temporal extent in August. The eastern U.S. fails to achieve the same level of temporal WD duration as the aforementioned western regions, though there is a clear annual cycle to WD with peaks in the summer and troughs in the winter. The southern Appalachian range and the Ozark Plateau are highlighted by the yellow and orange shading that appears in the JAS (July, August, September) plot of Figure 3, though it becomes apparent that elevation and surface roughness length are not the sole drivers of WD frequency due to the moderate positive anomalies (displayed in magenta in Figures 4 and 5) over the Gulf of Mexico and along its coastal plain in Louisiana, Mississippi, and Alabama. Viewing the climatology and anomaly plots holistically, one can identify that both the extent and magnitude of positive WD anomalies are greatest in the summer months, with a general minimum in the winter.

Plotting the spatial mean of WD days per month as a fraction of total days in each month reveals this annual cycle, the complete time series of which is included as Figure 6. The solid magenta line tracks the fraction of WD days in each month for all locations and shows annual peak fractions around August and minima during the winter and/or spring. The spatial averaging removes information about the location and extent of WD events, but is useful to characterize the dynamics of WD across longer time scales and identify individual months with anomalously high occurrence of WD. The dotted grey line shows the linear trend of WD during the time domain and has a slope very near zero, suggesting that there is no significant temporal trend for spatially averaged WD. There are, however, six outlying months where the average fraction of WD days exceeds 0.20, which all occurred during August. The variability in spatially averaged WD severity during August, the peak month, is captured in Figure 7, though as with the complete time series, the linear trend is constant. Wind Drought lacks a significant long-term directional trend in the spatial averages of all months as well as the peak month, August, which suggests that the influence of anthropogenic climate change on WD occurrence is negligible for the entire spatial average. The spatial anomalies for the six outlying months with the greatest fraction of WD are analyzed in detail in the next section.

### 3.2 Selection of Extreme Historical WD Events

The top six individual months that had the greatest spatially averaged fraction of WD days per month all occurred during August, which was determined to be the peak month for the WD climatological cycle. These months experienced extreme positive WD anomalies, exceeding seven days for some locations. In descending order, the years which experienced the highest August WD were 2005, 1990, 1996, 1983, 2014, and 1984. Plots of the WD anomaly for each outlying month are included in Figures 8 - 13. Each example illustrates one or more areas

throughout CONUS experiencing moderate to extreme WD exceeding 7 days per month. It is useful that all examples are from the same month at the peak of the annual WD cycle due to the greater prevalence of WD and its heightened variability in the summer months. The regions impacted by persistent WD in each outlying month vary in location and spatial extent, likely the product of a combination of atmospheric factors. Comparing the prevailing weather patterns and teleconnection regimes during each month for locations with anomalously high WD serves to identify potential physical factors that contribute to WD, which are examined on a theoretical basis in the Discussion.

### 3.3 Principal Component Analysis of Wind Drought

The monthly WD data was normalized and centered to perform Type I PCA with the goal of identifying patterns of space-time variability within the WD data field. With 4600 grid point locations and 42 (126) observations per month (season), PCA was performed separately for each month and season for  $n = 10$  components. Each resultant Empirical Orthogonal Function (EOF), or eigenvector, is by definition uncorrelated to the others and is expressed in the axis of its corresponding principal component (PC). The equation governing this analysis,  $U = XW$ , relates the PCs (columns of  $U$ ) to the product of the scaled WD data matrix ( $X$ ) and the EOFs (columns of  $W$ ). The monthly and seasonal EOFs were determined for all 10 components using singular value decomposition (SVD) of the covariance matrix of the scaled WD data. To inform the proper number of PCs to retain, a scree plot was generated for each month and season. The location of the “elbow” or sharpest bend in the scree plot is commonly used as a heuristic for PC retention, and a sample scree plot from the JAS season is included as Figure 14. The elbow is located after PC2, with the following PCs each explaining less than 2% of the total variance. Scree plots for each month and season share generally the same shape, with the variance

explained by the first PC ranging from 0.7249 (February) to 0.7934 (August). PC2's explained variance ranges between 0.018 (August) and 0.0324 (February). The decimal values indicate the fraction of the total variance within the WD dataset that is explained by each PC, or equivalently the eigenvalues of the covariance matrix of X. By retaining the first two PCs, between 75% and 80% of the variance is explained. The following correlation analysis of PCA results focuses on the EOFs for the first two PCs, and it should be acknowledged that although this application of SVD and PCA neglects to offer any explanation up to 20% of the variance within the data, meaningful correlations and conclusions can be drawn from the ~80% variance explained by the retained PCs.

### 3.3.1 Examining PC Correlation Patterns with WD Anomalies and $Z_{250}$ Anomalies

The 4600 elements of each EOF are referred to as the spatial loadings corresponding to each of the retained PCs. The monthly and seasonal loadings for both PCs are plotted in Figures 15 - 18. The PC1 monthly and seasonal loadings closely mirror the climatologies plotted in Figure 2 and Figure 3 with red (blue) loadings corresponding to high (low) monthly mean WD days. This observation allows the conclusion that red (blue) shading patterns in PC2 are also associated with increased (decreased) WD frequency. Patterns for both PCs are uncorrelated by definition and reflect distinct influences on frequency of WD reduced along the time dimension. PC2 loadings show broader dipole structures spanning the spatial domain, as well as significantly more locations that experience loadings with opposite signs across months and seasons. Within the Great Plains, seasonal differences in PC2 loading sign between AMJ and OND emerge from the noisier patterns specific to each month, evidence suggesting the existence of an intra-annual pattern for this region with a generally windier and less WD-prone climate. Further conclusions can be drawn by correlating the scaled WD data (grouped by both month and season) with the

time series describing the principal axis of each PC. This enables the projection of the eigenvectors from PCA onto the scaled WD data, and the agreement between them can then be calculated for each month and season. The components of the PC time series, which can equivalently be referred to as the right singular vectors of the scaled WD data, were multiplied by a factor of -1 to have the coefficient for a correlation with increased (decreased) WD be negative (positive), following the implicit logic that more WD equates to less wind. Any proposed physical cause of increased WD in a region must necessarily decrease the average wind, and to discuss potential causes for *decreased wind* in terms of *increased WD* while displaying correlations with increased WD as positive introduces unnecessary confusion. So, while the text will continue to utilize WD as the variable of interest, the correlation figures express positive correlations with WD with negative coefficients and tan shading, and inverse correlations with positive coefficients and teal shading.

Figures 19 – 22 show the values for the Pearson correlation coefficient between the PC time series and the time series for the scaled WD days per month value at each location. The strongest correlations in both directions exhibit the darkest colors, and the discussion of the patterns shown will favor the monthly and seasonal patterns that are correlated most strongly. For PC1 (Figures 19 and 21), the western U.S. shows a moderate correlation with increased WD in the winter months. The broadest correlation for the pattern described by PC1 emerges in the JAS seasonal plot (third panel of Figure 21) over the eastern U.S., and in particular the southern Appalachians, Ozark Plateau, deep south, and Gulf of Mexico. The seasonal peak of the annual WD cycle also shows moderate correlation with increased wind drought at elevation in the west as well, in the Cascade, Rocky, and Sierra Madre Occidental mountain ranges. Looking to PC2 shows stronger correlations on the seasonal time scale (Figure 22), with an enhanced WD signal

for the eastern U.S. in AMJ and a suppressed signal in JAS, the latter of which is the inverse of the pattern in PC1 (Figure 21). The enhanced drought signal peaks in May, the strength of which dominates a slight correlation with suppressed WD in June for the northeast. Similarly, correlations with suppressed WD in April and June for the Pacific northwest and west, respectively, interfere destructively with the rest of the AMJ correlations to create a weak, noisy pattern in the northwest for that season. The December and January plots for PC2 (Figure 20) identify a strong correlation with suppressed WD in the northwest, also at odds with the signal from PC1 in Figure 19.

Further correlations of the WD PC time series with 250 hPa geopotential height ( $Z_{250}$ ) anomalies as a proxy for jet stream structure and positioning displayed in Figures 25 – 28. These plots show  $Z_{250}$  anomalies correlated with an enhanced WD PC1 pattern in the summer months throughout the domain and in the northwest from October through February. A weak inverse correlation between  $Z_{250}$  and PC1 is present over the northeast in the winter months as well. The  $Z_{250}$  anomalies and PC2 show strong correlations in the seasonal plots of Figure 28, with the data correlating with suppressed WD throughout for AMJ and a weaker correlation in the eastern U.S. for JFM. On the other hand, JAS and OND anomalies show strong correlation with suppressed WD, with this signal also appearing over the western U.S. during JFM. The monthly plots for  $Z_{250}$  anomalies and PC2 in Figure 26 exhibit a range of dipole patterns with moderate coefficient extrema and lesser spatial extent of the strongest correlations, suggesting that aggregating the  $Z_{250}$  anomaly data into seasons improved its fit to the PC2 time series, and that the WD variability captured by PC2 is better correlated with jet stream structure on a seasonal time scale. Patterns within PC1 also appear to persist on a longer than monthly time scale, but generally are not as well aligned with the grouping of months into seasons to show up strongly within the

seasonal plots, especially AMJ and OND. Synoptic-scale effects of anomalous jet stream structure include shifted storm tracks, as well as influencing surface winds by shifting the positions of surface circulations induced by convergence or divergence of air aloft. Large-scale dynamics within the atmosphere are the main influence on subseasonal to seasonal jet stream structure, and a selection of northern hemisphere teleconnection patterns are examined to identify further correlations within the data.

### 3.3.2 Examining Correlations Between Teleconnection Patterns and WD Anomalies

Three leading modes of atmospheric teleconnection patterns are considered in this analysis due to their well-documented influence on North American weather and climate: the El Niño Southern Oscillation (ENSO), the North Atlantic Oscillation (NAO), and the Pacific/North American pattern (PNA). (Null, 2022; Osborn, 2010; Mitchell, 2010) The correlation coefficients between the NIÑO3.4, NAO, and PNA teleconnection indices and monthly WD anomalies are shown in Figures 29 – 31. Unlike the correlation coefficients between WD anomalies and PC time series in previous figures, no inversion was performed on the pattern index time series. Locations where the monthly WD anomalies correlate directly (inversely) with the index have positive (negative) coefficients and are shaded tan (teal). Regions exhibiting correlation values exceeding 0.4 in absolute value are uncommon in most months for all indices, which reflects the complex interplay of small- and large-scale atmospheric factors which govern near-surface winds and the difficulty that arises when attempting to describe direct relationships between variables over time.

In the ENSO plot (Figure 29), there is a moderate correlation between the NIÑO 3.4 Index and WD conditions for the western US during April through June, and similar signals for the northeast U.S. in June and September and the Ozark plateau in January, February, and

November. The NAO plot (Figure 30) shows a broad region of inversely correlated WD anomalies over the Northern Great Plains, Great Lakes, and northeast for February, with slightly weaker inverse correlations in March. Positive correlations between NAO and WD anomalies exceeding 0.4 are exceedingly scarce, reflecting a significant amount of noise within the correlation data. The PNA index correlates positively with WD anomalies over portions of the western US including Utah, Colorado, Idaho, and Wyoming in January, February, March, April, June, and November, with the strongest signal in January (Figure 31). These three figures are useful to characterize the level of alignment between the time series of the teleconnection index and WD anomaly at each location. However, they fail to offer information on the effect of the opposite modes on WD anomalies. Due to the low correlation coefficients between the monthly anomalies and full teleconnection indices, a different analytical strategy must be employed.

#### 3.4 Analysis of Composite WD Anomalies under Moderate to Strong Teleconnection Modes

Composites for moderate to strong instances of the positive (negative) mode of each index were compiled by selecting months with index values above 1 (below -1). The aggregated monthly WD anomalies for each mode of the ENSO, NAO, and PNA composites are shown in Figures 32 - 37. Positive monthly WD anomalies are largest under El Niño regimes (Figure 32, n = 55 months), with strong positive anomalies in the spring in portions of the Rocky Mountains and the western U.S. and positive anomalies for the Ozark Plateau and Appalachians in May and July. Western Mexico and Baja California exhibits highly anomalous WD in April under El Niño, while coastal southern California experiences strong positive WD anomalies in response to April and May El Niños. The upper Great Lakes region experiences moderate positive WD anomalies from June El Niños. On the other hand, the Cascade region experiences a deficit in WD under El Niño conditions for January, February, and April. El Niño conditions also yield

negative WD anomalies for the desert southwest in July and the Appalachians and deep south in August. The La Niña composite (Figure 33, n = 63 months) shows anomalies with generally smaller magnitudes and a larger share of green shading than El Niño. Negative WD anomalies dominate the western U.S. for March and November in addition to the Gulf of Mexico in July and, to a lesser extent, September under La Niña regimes. Increased La Niña WD anomalies appear in coastal Oregon and Washington in June and near Florida in May.

Composites for the NAO (Figures 34 – 35) show moderate anomalies of 2-5 more WD days per month during +NAO (Figure 34, n = 83 months) over the Gulf of Mexico and deep south during July, and one- to four-day positive anomalies for +NAO July's in the entire domain excluding the Great Plains and California. March and October also show slight positive WD anomalies over California and the deep south associated with the +NAO phase. The positive composite uncovered weak WD anomaly patterns throughout CONUS for February, April, June, November, and December. The negative composite (Figure 35, n = 85 months) yields strong positive anomalies for September over the northwest and Idaho in particular, though much of the western U.S. experiences positive WD anomalies in Septembers under -NAO. The July WD anomalies in the southeast and the eastern Gulf of Mexico range between 1 and 3 additional days under -NAO, and combined with the +NAO anomalies for the same regions this suggests that a moderate/strong positive *or* negative phase of the NAO contributes to elevated WD. Remaining anomaly patterns within the -NAO composite are weak, with minor negative WD anomalies (and an inverse association with WD) present for the southeast during June and August, the Cascades in February, and southern California in January, February, and April.

January exhibits the strongest positive WD anomalies for the +PNA composite (Figure 36, n = 89 months) primarily over the western U.S., with the highest anomalies from 3-7 days in

the mountainous regions of Idaho, Utah, and Colorado and weaker positive anomalies in the southwest and southern California. June and July show weak positive anomalies for the desert southwest as well for +PNA. Moderate negative WD anomalies are present for coastal southern California in March, offsetting moderate positive anomalies in the northern Rocky Mountains. The negative phase of PNA (Figure 37, n = 91 months) has few instances of positive composite WD anomalies, confined to the Appalachians and Pacific northwest during May, with weak positive anomalies for California in December as well. Negative WD anomalies appear in the - PNA composite over the western US in January, the Ohio River Valley in August, and Mississippi and Alabama in July.

## 4. DISCUSSION

### 4.1 Interpretation of Results from PCA and Correlation Analysis

The first and perhaps most trivial of observations is that the greatest variability in WD on a monthly and seasonal basis is present in areas that climatologically experience at least a couple of days per month with WD conditions. WD is exceedingly rare in locations with persistent windy conditions (shown in Figures 2 – 3 with dark green shading) such as the Great Plains and upper Midwest, with this predominantly wind-rich pattern appearing in blue in the PC1 loadings shown in Figures 15 and 17. PC1 correlations for this region are low in magnitude and variable in sign, suggesting that the dominant drivers of WD variability elsewhere in the domain are neither enhancing nor suppressing WD in most of the U.S. interior. This region's relative independence from WD patterns at large is attributable to its flat, open terrain that is conducive to wind speeds sufficient to drive wind turbines even during calmer than average conditions. Over Florida and the Gulf of Mexico, climatological WD tracks with the evolution of loading patterns across the southeastern U.S. during the spring and summer. This region exhibits the

most pronounced annual cycle of PC1 loadings as shown in Figures 15 and 17, turning from blue to red and indicating enhanced WD for the summer months, which is confirmed in the anomaly plots in Figures 4 – 5. It should be noted that while the Sierra Madre Occidental range exhibits higher positive WD anomalies for JAS, PC1 loadings for that region are positive for all months, indicating greater WD variability throughout the year. Darker brown shading for both regions during JAS in Figure 21 represents better agreement between PC1 and the WD data and suggest that PC1 explains enhanced WD well during JAS in those areas. Contrasting correlations between PC2 and WD data in Figure 22 for the same regions during AMJ and JAS illuminates an opposite pattern, in which strong correlations with enhanced WD appear in AMJ but equally strong correlations with suppressed WD appear in JAS. The suppressive pattern (in teal) experiences its maximum during JAS and September in particular, which coincides with the peak of tropical cyclone season for the Atlantic basin. Tropical cyclones have a tremendous effect on surrounding weather patterns, with their deep sea-level pressure signatures generating large-scale cyclonic flow around the central depression and inducing calmer anticyclonic surface flow in surrounding regions. Wind speed variability over CONUS is driven by midlatitude cyclone tracks, but since tropical cyclones are warm-core systems and produce differing upper-level circulations than midlatitude cyclones, signals for this proposed mechanism do not appear strongly in correlations between WD and  $Z_{250}$  anomalies.

Following the findings of Pryor et al. (2018) that seasonal wind speed variability is driven by tracking of midlatitude cyclones, the correlation plots of WD PCs and  $Z_{250}$  anomalies in Figures 25 – 28 illustrate how well changes in atmospheric structure aloft agree with shifts in WD occurrence throughout the domain. The dipole in correlations with PC1 during the winter months, with enhanced WD for the northwestern U.S. and suppressed WD for the northeast,

suggests that the more meridional winter structure of the jet stream pattern favors cyclogenesis east of the Rocky Mountains and limits winter WD for the northeast while enhancing WD in the northwest. The PC1 correlations support this finding since cyclones developing over the central U.S. and tracking toward the northeast would bring increased winds to the area and suppress WD. This pattern subsides in the summer months under upper-level flow regimes that are generally more zonal. Midlatitude cyclones are more numerous in the winter months, and more frequent passing of storm systems brings windier conditions. As continental cyclogenesis wanes in the summer months, high pressure systems stifle surface-based convection and bring calmer conditions, increasing the favorability for WD episodes. The JAS panel in Figure 27 illustrates this impact, with positive height anomalies corresponding with increased wind drought (yielding negative correlation values as detailed in Section 2.1) during JAS throughout the domain.  $Z_{250}$  correlations for this season surpass -0.4 throughout the Great Plains, where correlations with PC1 in other seasons do not exceed  $\pm 0.2$ . The summer months experience the most pronounced large-scale ridging of the jet stream, which is seen to be associated with calmer winds and elevated WD. Geopotential height patterns for 250 hPa are shown in Figures 23 – 24, where the shape of the “zero” contour in white reflects the mean positioning of the polar jet for each month and season.

PC2 shows greater variability across months, coalescing into domain-wide patterns when aggregated by season. Strong correlations between  $Z_{250}$  anomalies and PC2 of the WD data for enhanced WD in AMJ and suppressed WD in JAS and OND suggest that the minor share of seasonal WD variability captured by PC2 is well explained by positioning of the jet stream and the resulting large-scale flow patterns. As captured by PC2, seasonal fluctuations in the jet stream’s positioning correlate with a net enhancing effect on WD in AMJ and a net suppressive

effect in JAS and OND. Recalling Figure 14, PC2 is responsible for only about 3% of the total variance in WD, compared to about 75% explained by PC1.

#### 4.2 Proposed Contributions from Climate Modes on WD prevalence

The goal of correlating monthly anomalies in WD with three atmospheric teleconnection indices was to identify how consistent the WD data at each location were with the manifold weather impacts of each pattern. The correlations between monthly WD anomalies and the time series for ENSO, NAO, and PNA indices fail to reveal strong domain-wide correlations but do illuminate several areas of enhanced agreement between WD anomalies and the teleconnection pattern of interest, as identified in Section 3.3.2. Conclusions can be drawn from the shading in Figures 29 – 31: Tan-shaded regions experience elevated WD as the index becomes more positive (and vice versa) while teal-shaded regions experience suppressed WD with a more positive index. Grouping the WD data by positive and negative modes for each index enables better diagnosis of their direct contribution to WD since the influence on North American weather regimes of each mode increases with its index's magnitude. Composites of months where each mode's index is beyond  $\pm 1$ , shown in Figures 32 - 37, express the averaged WD anomalies by month. El Niño (Figure 32) contributes both positively (purple shading) and negatively (green shading) to WD anomalies depending on the location and month. Spring months have largely positive WD anomalies during El Niño, though the sign of the WD anomalies is highly spatially variable. January and August El Niño events tend to have a more suppressive imprint on WD, shown in green. Months during La Niña experience more meager WD anomalies compared to El Niño, with the only strong positive WD anomalies arising in coastal Oregon and Washington during June and the Gulf of Mexico during May. Lightly suppressed WD is the more broadly observed impact of a La Niña episode, especially in the Gulf

of Mexico in July and September, much of the southeast in June, August, and September, and over the western U.S. during February, March, and November. The high spatial variability in WD anomalies for El Niño and La Niña composites points to shifts in storm tracking caused by disturbed atmospheric circulation under each regime. ENSO's impact on the Walker Circulation over the tropical Pacific and associated volatility in the structure of the subtropical and polar jet streams results in storm tracks that are displaced from climatology, leading to strong positive and negative WD anomalies for the spring and summer months.

The North Atlantic Oscillation composites in Figures 34 – 35 show WD anomalies that lie in a narrower range than the ENSO composites but do not show as much variation on a regional level. The positive phase, reflecting above-average geopotential heights and temperatures over eastern North America, is associated with at least two more WD days in July for the Gulf of Mexico, with the majority of the western (eastern) U.S. experiencing 1-2 additional WD days during January, March, August, and October (January, July, August, September, and October) during +NAO. The southeastern U.S. exhibits moderate positive WD anomalies on the order of 3 days per month from July through October, which supports the hypothesis that the altered flow from +NAO influences the favorability for WD conditions. The negative phase composite shows strong positive WD anomalies in September for the northwestern U.S. and the Gulf of Mexico, with weaker positive anomalies in January for the Pacific northwest. Contrasting the two phases by month shows that +NAO results in slight positive anomalies for the southern half of CONUS during January through June and negative anomalies for the northern half, and the anomaly patterns are flipped for -NAO such that the northern half of the United States experiences slightly positive WD anomalies in the first 6 months of the year. The greater spatial coherence of WD anomaly patterns for the NAO

composites suggests a less pronounced localized imprint of the NAO regime on WD but enables more reliable diagnosis of WD patterns tied to the NAO. Both phases of the NAO shift the location of the jet stream, reinforcing the hypothesis that the majority of seasonal WD variability is due to effects on predominant storm tracks, driven by the structure of the jet stream and other upper-air dynamics.

The Pacific/North American pattern strongly impacts the Pacific jet stream structure and weather patterns over CONUS, with composite monthly WD anomalies for the positive phase shown in Figure 36 almost exactly mirroring the negative phase with inverted anomaly signs. The greatest positive WD anomaly for the +PNA phase is over the Pacific northwest in January, a location that tends to receive above average precipitation totals on top of warmer surface temperatures throughout the western U.S. The negative phase shows the opposite pattern for January, with suppressed WD in the western U.S. in addition to suppressed WD in the southeast for July and August. On the aggregate, +PNA is associated with moderately positive WD anomalies and -PNA has a more suppressive influence on WD. Slight positive WD anomalies during May for the northwest and southeast as well as during December for California are the most prominent instances of enhanced WD for -PNA, where WD anomalies are primarily neutral or negative.

#### 4.3 Inspection of WD Anomalies During Months with Extremely High WD

Six individual months were identified as having anomalously high prevalence of WD, determined by the spatial average of WD days per month in Figure 6. These extreme outliers all occurred during August, during the years 2005, 1990, 1996, 1983, 2014, and 1984, in decreasing order of spatially-averaged WD fraction. August is the peak month in annual WD climatology (recall Figure 2), so positive anomalies shown in purple in each panel of Figures 8 – 13

compound with climatological WD values, with the darkest purple shading corresponding to an additional week under WD conditions. Since the domain covers large portions of open ocean, one must consider that a high anomaly of WD days does not necessarily correspond exactly to the overall negative impact on wind energy generation potential over land or near shore, where the vast majority of current wind energy infrastructure is located.

August 2005 shows large regions of positive WD anomalies in the southeastern U.S. and Gulf of Mexico, with strong but less uniformly distributed positive WD anomalies in the Rockies and desert southwest. August 2005 ranked among the top 10 wettest Augusts on record for the eastern Texas, Louisiana, and the Ozarks, and in the top 10 warmest months for the southeast (NOAA NCEI, 2005). Hurricane Katrina impacted the Gulf of Mexico region in the last week of August 2005, contributing to the above average observed precipitation. Tropical cyclones bring increased wind speeds and suppress WD due to strong local pressure gradients as the storm deepens. However, a counteractive impact of tropical cyclone passage on WD is the induced calmer conditions in surrounding areas, as well as increased favorability for WD conditions prior to the storm's passage arising from the low wind shear that is critical to tropical cyclone intensification. August 2005 experienced a neutral ENSO and PNA along with a moderate +NAO, and the resulting patterns in WD anomalies match the August panel in Figure 34, with weaker magnitudes due to averaging. +NAO is associated with higher geopotential heights over the eastern U.S., contributing to anomalous ridging over the eastern U.S. and a longwave trough extending upstream, stymying midlatitude cyclone formation over the southwestern U.S. and west of the Rockies (NOAA NCEI, 2005). The perturbed jet stream structure under this regime creates the correct conditions for WD in the form of displaced storm tracks in the western U.S. and anomalous ridging and calm periods. From a renewable energy perspective, atmospheric

ridging poses less of a threat to S+W RD due to broad anticyclonic circulation at the surface and high sea level pressure (SLP), causing mass divergence at the surface and subsiding air, which limits cloud cover and aids solar resource availability.

The second highest spatially averaged WD fraction occurred in August 1990, portrayed in Figure 9. WD anomalies are most significant over the western Atlantic and Gulf of Mexico, in addition to much of the Appalachian range through the northeast U.S., with a particularly strong episode in Ohio. The southeast experienced above average temperatures and dry conditions, while a northward displacement in the Pacific jet caused positive height anomalies and enhanced WD in the northwest, likely through both the ridging and storm track mechanisms (Ropelewski et al., 1993). ENSO was neutral, though warming in advance of the strong El Niño of 1991-1992 (Null, 2022). A moderate -PNA and weak -NAO also influenced a split flow pattern, diverging over the Ohio River Valley and feeding ridging-enhanced WD anomalies (Osborn, 2017; Mitchell, 2010). Regions of western Mexico windward of the Sierra Madre Occidental range experienced increased WD under a wet and cool weather regime, fed by tropical moisture transported northward with the displaced westerlies.

The dominant pattern in WD anomalies for August 1996, shown in Figure 10, is for strongly enhanced WD over the Ozarks, northern Missouri and Iowa, the Ohio River Valley, the Gulf states, the Appalachian range, and entire eastern seaboard. East of the Great Plains, the month was cloudy, cool, and wet with upper level troughing (NCEP CPC, 1996). After 11 months of wetness (125%–165% of normal) preceding August 1996 causing high crests in Illinois, much of the Great Lakes, Appalachians, and northeast had saturated soil and a moist atmosphere which limited diurnal fluctuations in temperature and prevented radiative-forced

convection thanks to latent heat (NCEP CPC, 1996). This enhanced WD pattern east of the Great Plains is influenced by deflected storm tracks and calm winds that accompany stratiform rain.

August 1983 (Figure 11) was the month with the fourth largest WD fraction and saw positive WD anomalies in much of the western U.S. and the Gulf states. It was the warmest August to date for Colorado and the state's sixth warmest in the period of record, 1895-2021 (NOAA NCEI, 2022). Precipitation for the west climate region in August was a record high, at 400% of the 20<sup>th</sup> century mean (NOAA NCEI, 2022). This confluence of warm and wet conditions is similar to the southeastern U.S. during August 2015. July-August 1983 was the driest two-month period for the southeast climate region, while August was the 11<sup>th</sup> warmest on record and under neutral ENSO and NAO, with weak -PNA (Null, 2022; Osborn, 2017; Mitchell, 2010). A persistent cyclone over eastern Pacific brought ample tropical moisture to the west and combined with elevated surface pressure and geopotential heights over the southeast to deflect storms northward and contribute to calm, clear-skied heat wave conditions in much of the southeast (Armstrong, 2017). Increased electricity demand from spikes in air conditioning during heat waves in conjunction with persistent WD strains power grids even further, and a diminished contribution from renewables threatens the ability of future grids to match power demand without advance preparation and sufficient electricity storage and transmission infrastructure.

The most recent example of extreme spatially averaged WD fraction is from August 2014, primarily affecting northern Nevada and Utah, Idaho, western Montana, and northwestern Wyoming, in addition to positive anomalies for the northern Great Lakes and central northern Mexico. The Northern Plains and Rockies had 276% of its average August precipitation, leading to its wettest August on record (NOAA NCEI, 2022). Monthly surface temperature anomalies between -1 and -2 degrees Celsius in the eastern U.S combined with slow-moving stratiform rain

systems and a 500-year northeast storm to contribute to enhanced WD over Maine, the Great Lakes and southern Canada (NOAA NCEI, 2022). Late August 2014 brought extreme heat to the Midwest and northeast, offsetting the cooler, wet pattern of the first half of the month and driving the positive WD anomalies.

The final extreme WD event occurred in August 1984, with much of the desert southwest experiencing strong positive WD anomalies in addition to the southern corners of the domain. The month had a moderate +NAO and +PNA, influencing the large-scale flow patterns that resulted in increased cloud cover and 150% of normal precipitation for the southwestern U.S (Osborn, 2017; Mitchell, 2010; NOAA NCEI, 2022). Flash flooding in central Utah was reported to have washed cars off the interstate on August 15<sup>th</sup>, 1984 (Alder et al., 1996). Wet soil and a saturated atmosphere stifle diurnal temperature fluctuation, which are typically very large in the southwestern summer, and suppress convection from sensible heat flux, leading to less windy conditions and elevated WD.

## 5. CONCLUSION

Wind Drought patterns are inherently noisy, due to the strong dependence on location-specific wind climatology and subseasonal to seasonal variations in large- and small-scale drivers of wind speed. Wind energy generation installations rely on consistent winds and minimal calm periods in order to supply renewably sourced electricity that meets growing demand. Previous studies have linked periods of extended low wind speed – defined in this study by a daily average wind speed below 3 m/s – to changes in midlatitude cyclone tracks and other sources of interannual variability including the El Niño Southern Oscillation, the North Atlantic Oscillation, and the Pacific/North American pattern. Principal Component Analysis and

correlations with 250 hPa geopotential heights (as a proxy for jet stream structure) and the three selected teleconnection patterns isolated by month and season revealed patterns in location and timing of enhanced WD events. Understanding the links between WD and other atmospheric variables of interest enables insights and predictions of WD prevalence based on their combined effects. The mountainous western U.S. has moderate WD occurrence year-round, while the eastern U.S. follows an annual cycle peaking in August. WD is rare in the Great Plains due to decreased surface friction and minimal momentum transfer to the surface. Averaged over the entire domain, there is no trend for increasing WD with time. Likewise, there is no linear trend in the magnitude of spatially averaged WD for Augusts throughout the time period, typically the maximum month in terms of WD occurrence. However, severe WD was found to occur more frequently with extreme weather patterns such as heat waves or anomalously high precipitation.

On a synoptic scale, WD shares a correlation pattern with the seasonal undulations in the jet stream and its routing of midlatitude cyclones. There is no single “recipe” for Wind Drought, but rather a range of patterns that enhance or suppress wind speeds near the surface, combining in location-specific ways. For certain months and locations, WD is correlated with fluctuations in the ENSO, NAO, and PNA indices. Composites of positive and negative modes identified connections with WD anomalies consistent with the typical impacts of each climate mode on large-scale flow patterns and weather effects. These impacts contribute to the overall environmental favorability for WD conditions, but the ultimate driver of seasonal variability in WD is the imprint of jet stream structure on wind conditions. When supportive large-scale conditions for WD coincide with other enhancing factors, extreme positive WD anomalies can result and pose a threat to the available supply of wind energy.

## 6. FIGURES

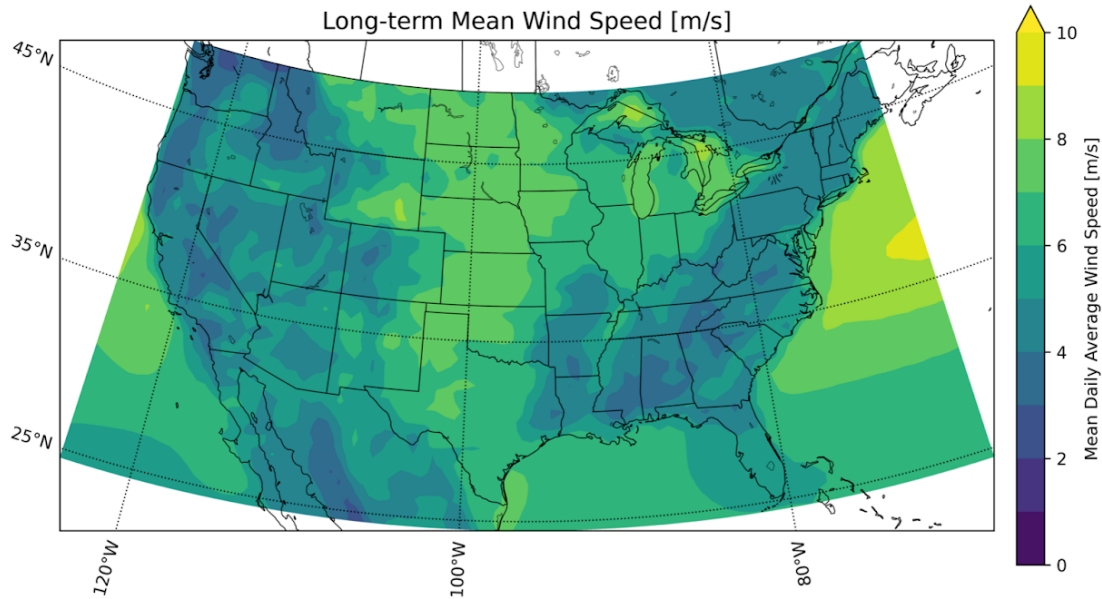


Figure 1. Annual wind speed climatology of the study domain (1980-2021) from MERRA-2 at 0.625 degree spatial resolution and one-hour temporal resolution.

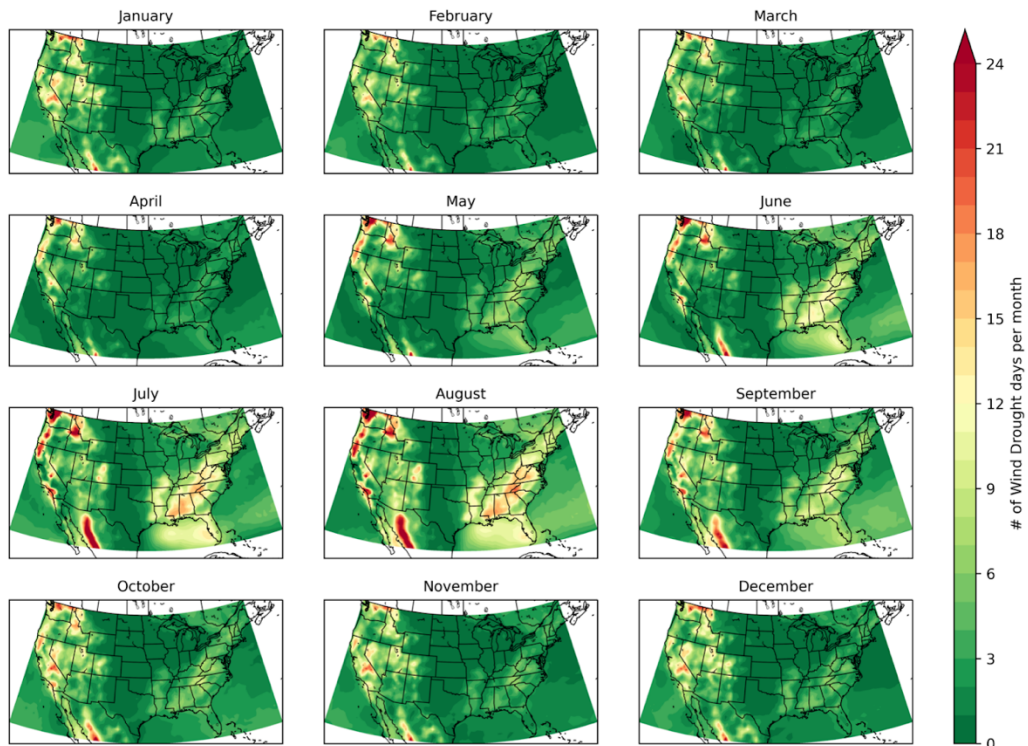


Figure 2. Monthly climatologies of WD days per month, i.e. Mean number of days with daily mean wind speed below the 3 m/s threshold. Green shading represents very few days of WD conditions and daily average wind speeds overwhelmingly above 3 m/s, while yellow and red represent more frequent occurrences of WD conditions.

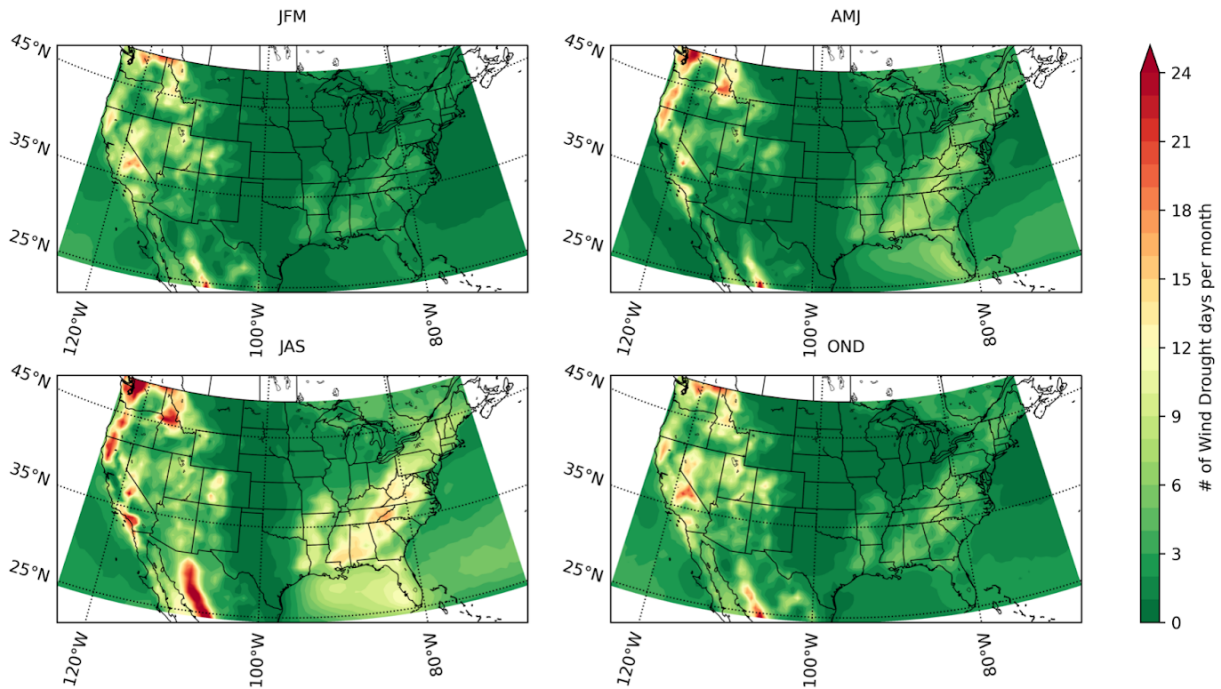


Figure 3. As in Figure 2 except for seasonal climatologies.

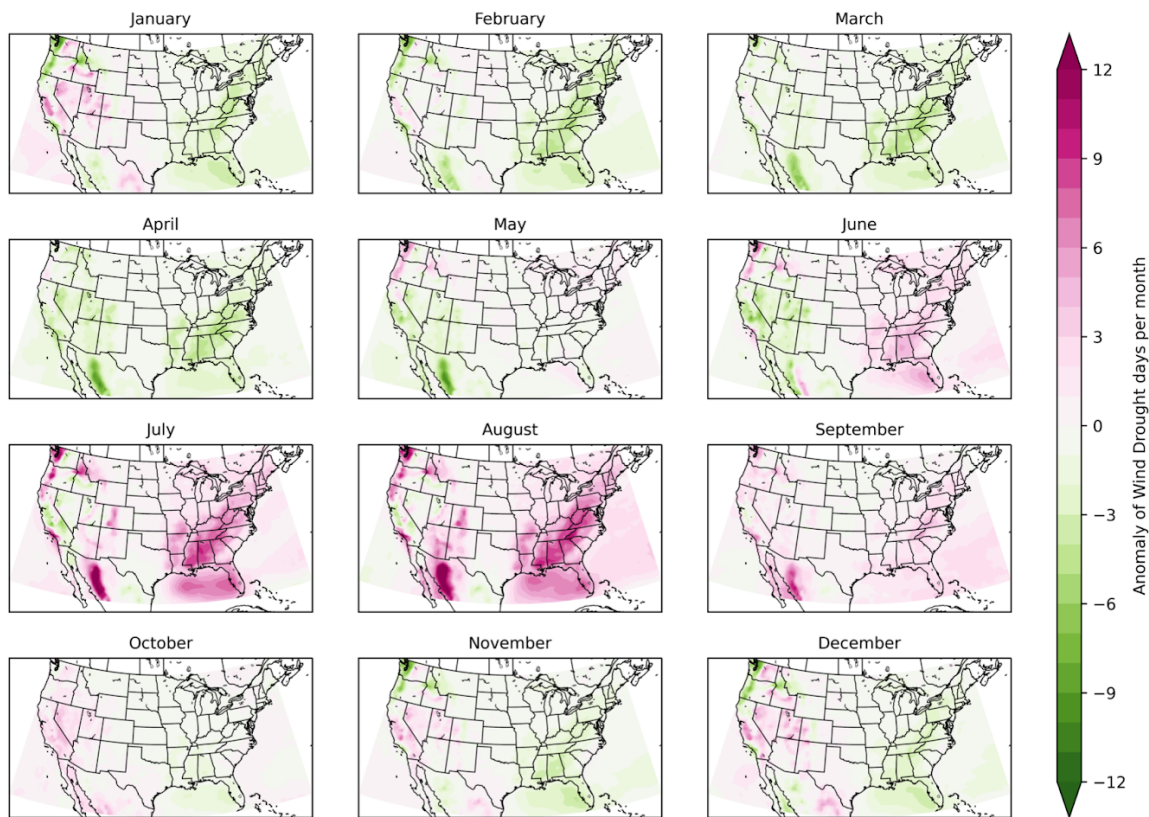


Figure 4. Monthly anomalies of WD days per month, i.e. average monthly departure from the long term mean of WD. Purple represents increased occurrence of WD conditions relative to the annual mean, and is most widespread in the summer months.

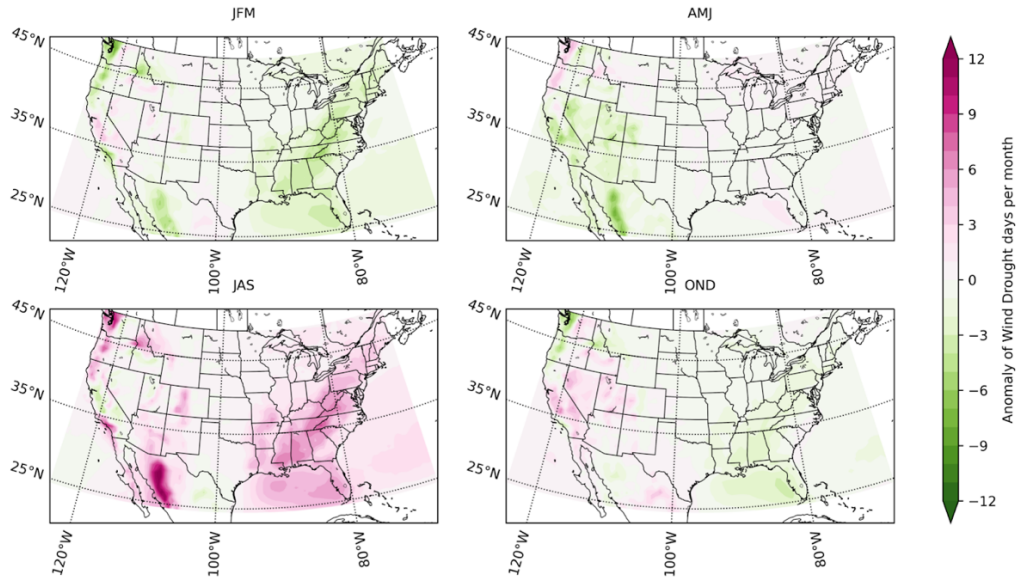


Figure 5. As in Figure 4 except for seasonal anomalies.

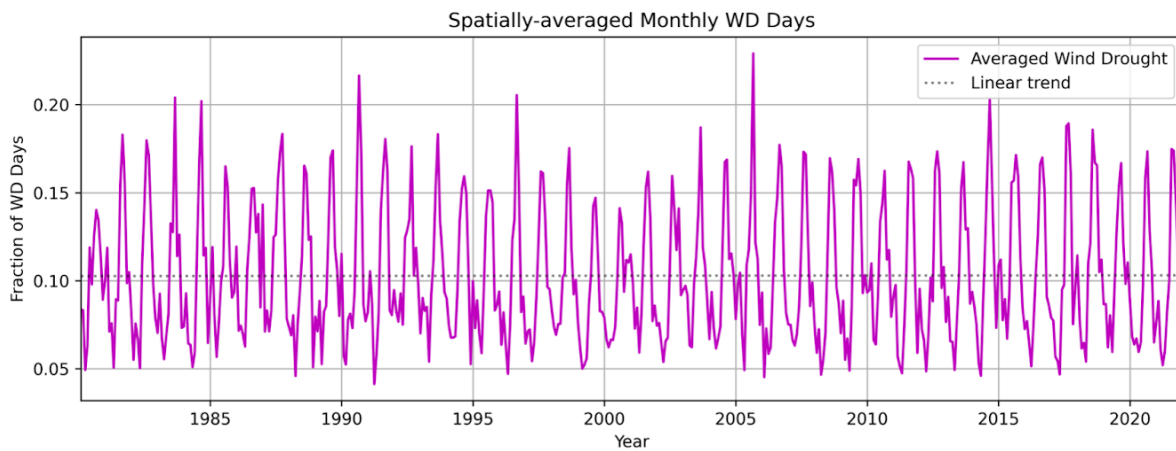


Figure 6. Time series displaying the spatially averaged days per month under WD conditions for all months in the analyzed time period.

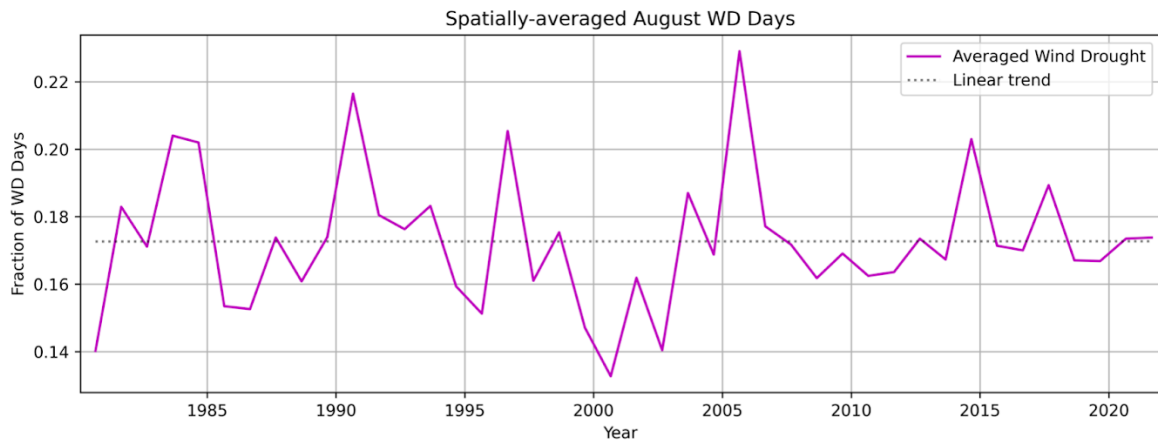


Figure 7. As in Figure 6 except for Augusts only.

August 2005 Wind Drought Anomaly

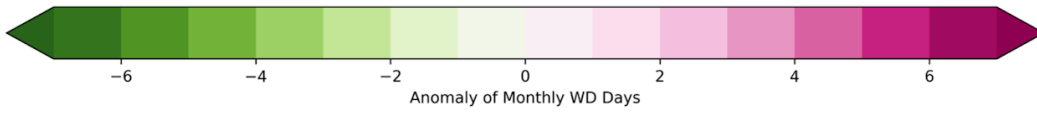
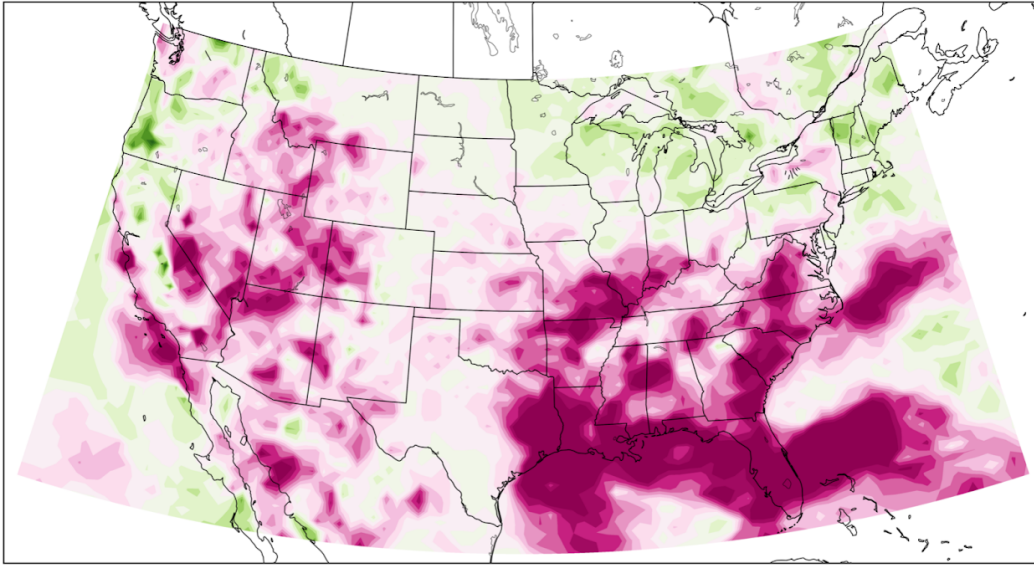


Figure 8. WD anomaly for August 2005.

August 1990 Wind Drought Anomaly

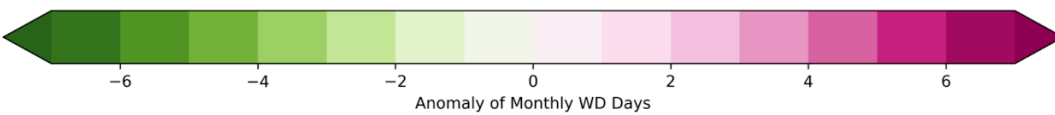
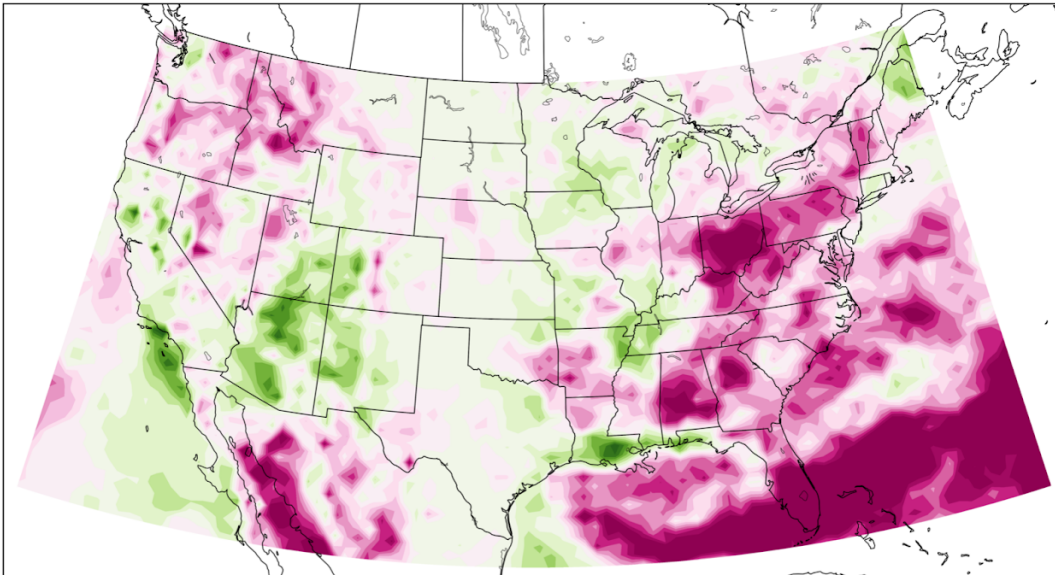


Figure 9. WD anomaly for August 1990.

August 1996 Wind Drought Anomaly

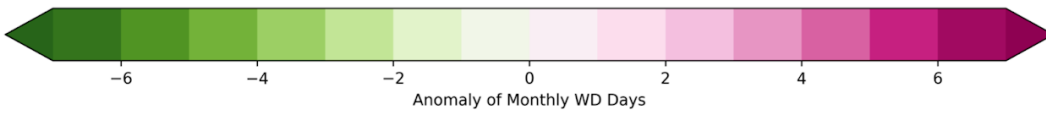
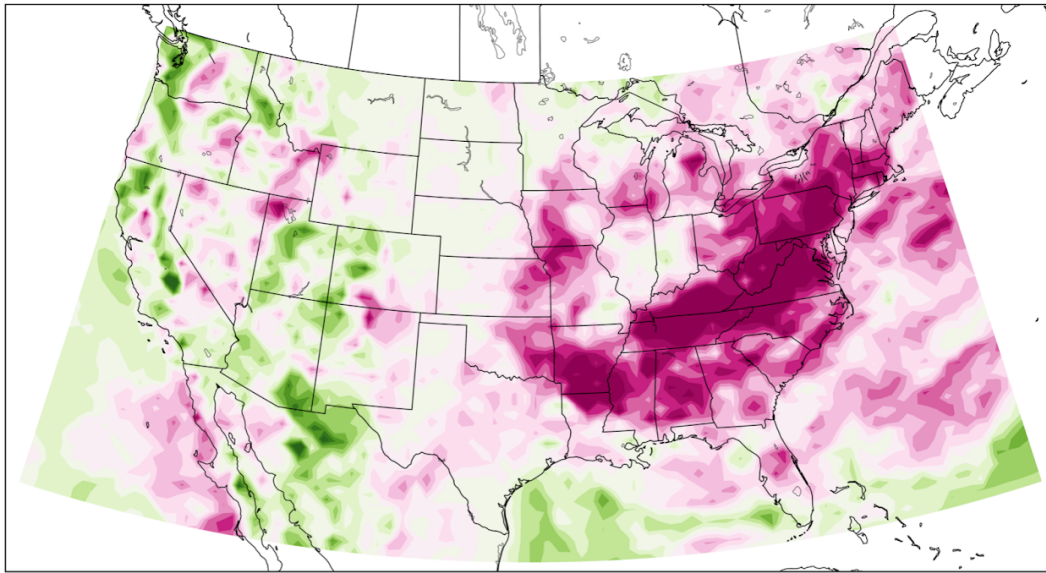


Figure 10. WD anomaly for August 1996.

August 1983 Wind Drought Anomaly

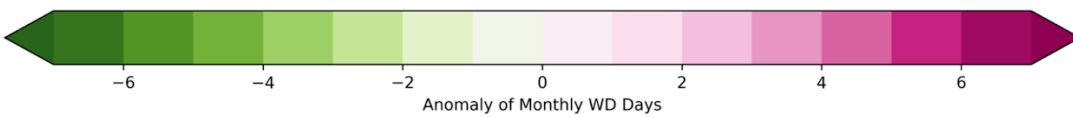
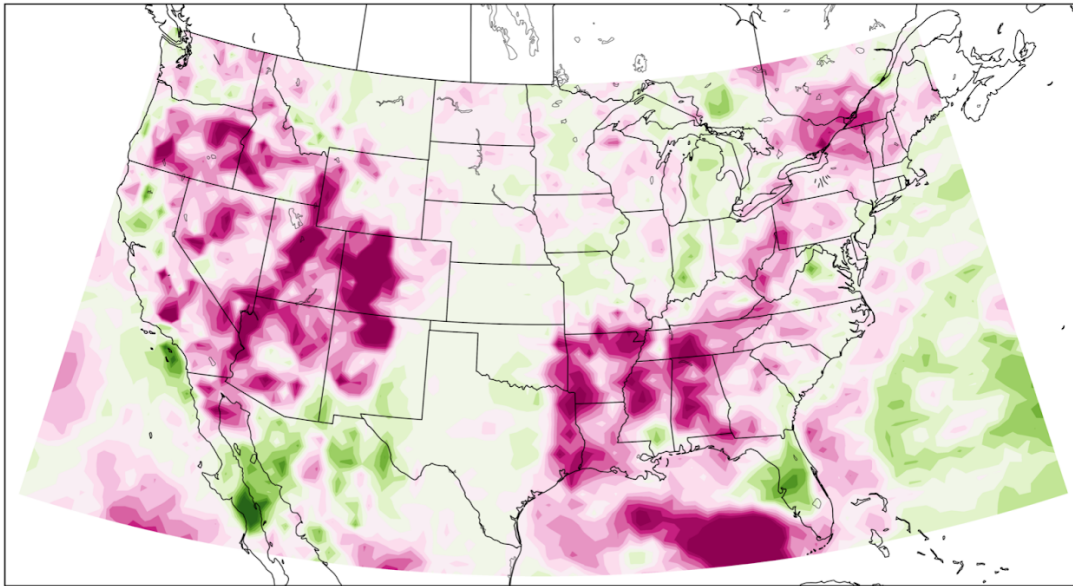


Figure 11. WD anomaly for August 1983.

August 2014 Wind Drought Anomaly

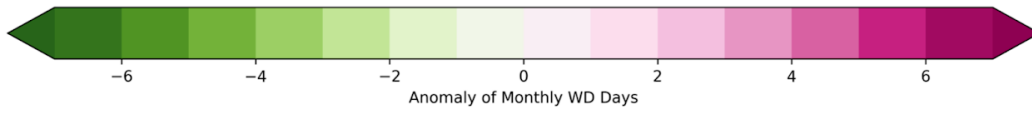
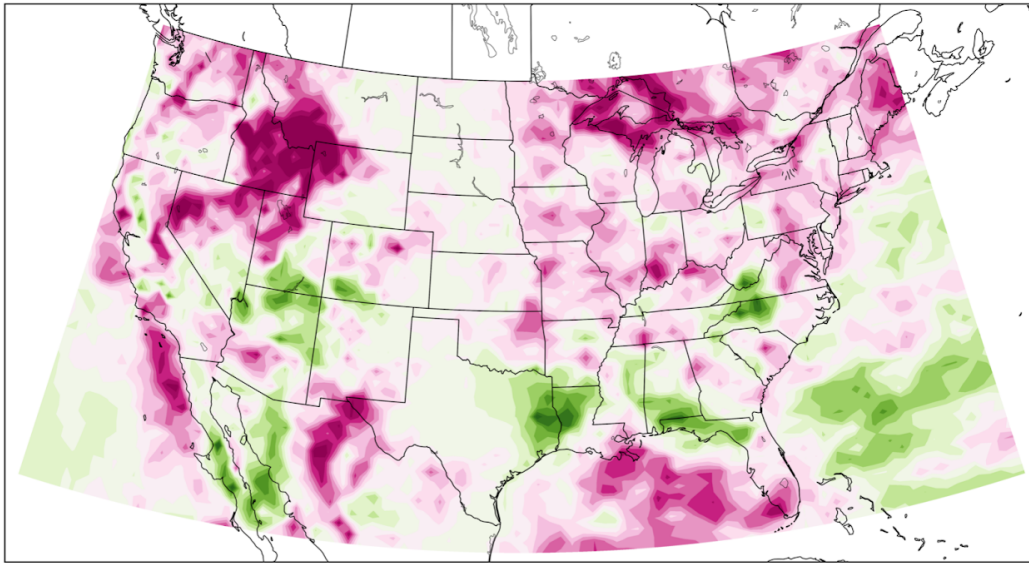


Figure 12. WD anomaly for August 2014.

August 1984 Wind Drought Anomaly

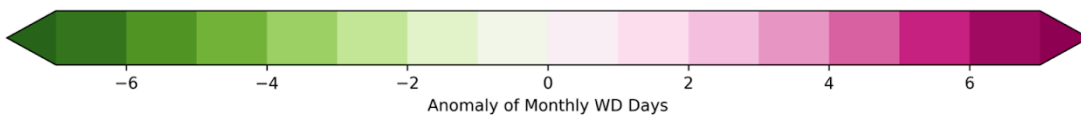
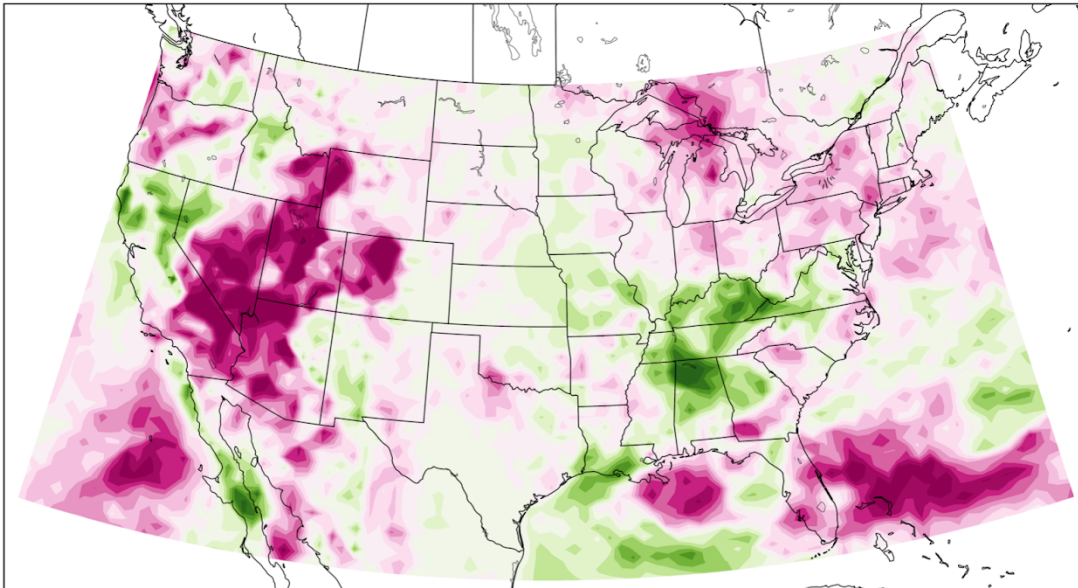


Figure 13. WD anomaly for August 1984.

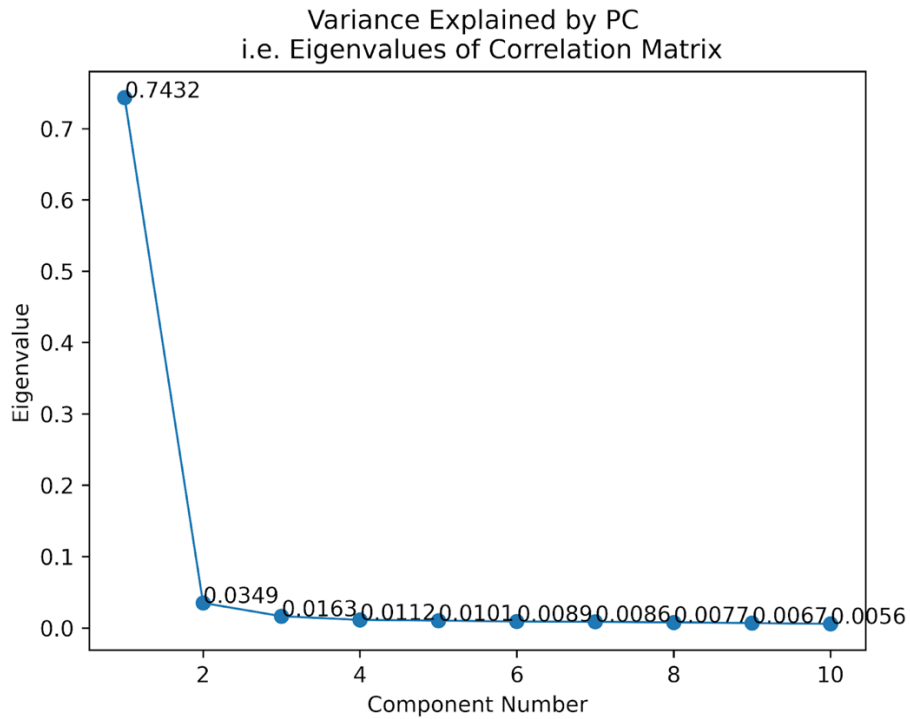


Figure 14. Scree Plot displaying the decimal share of the total variance within the WD data explained by the first ten principal components. Note the location of the graph's "elbow" after PC 2, which informed the decision to retain only the first two principal components for analysis.

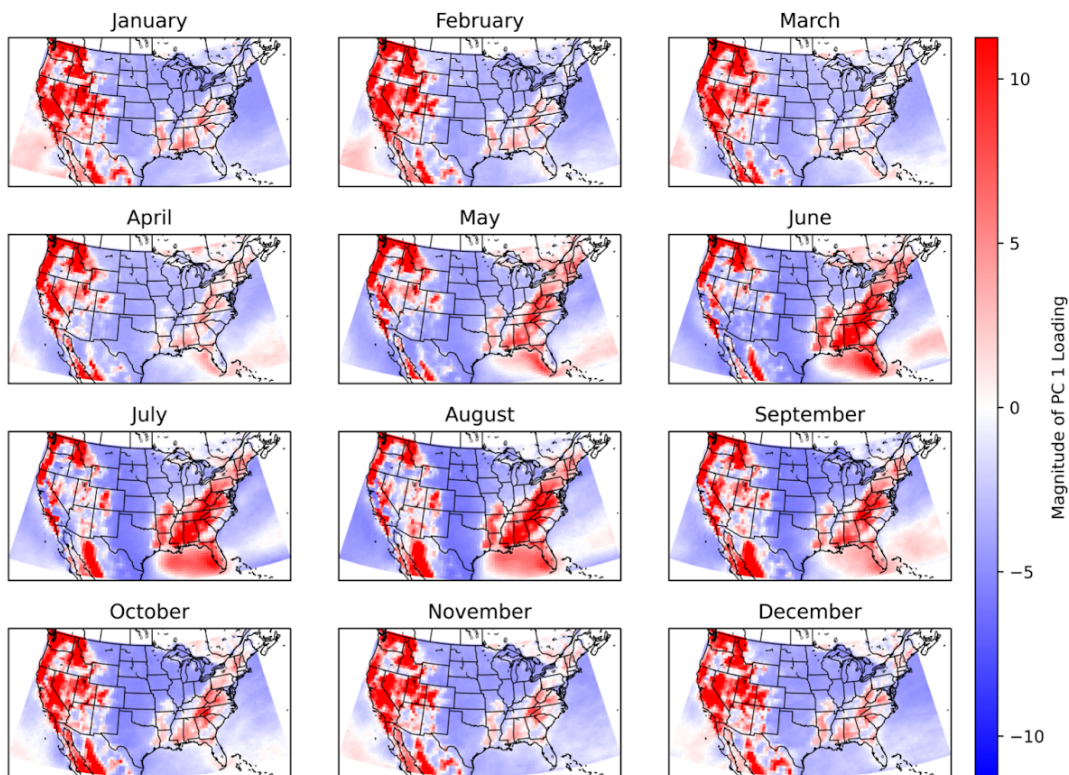


Figure 15. Spatial loading patterns for the first principal component of WD for each month. Units are arbitrary.

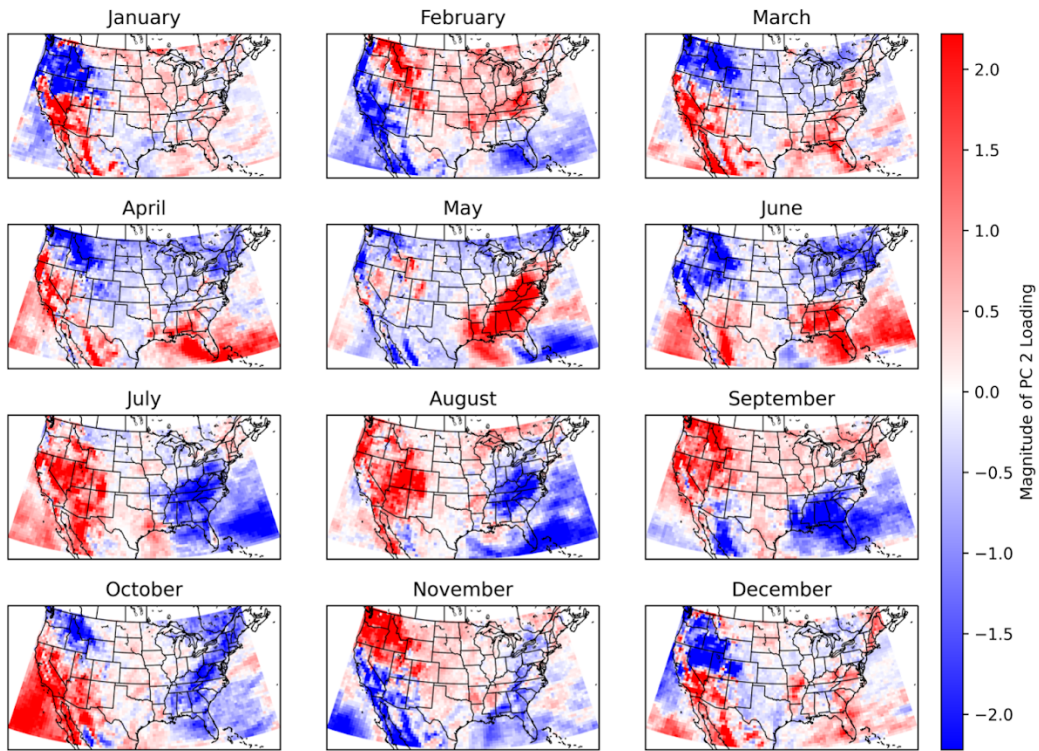


Figure 16. As in Figure 15 except for the second principal component

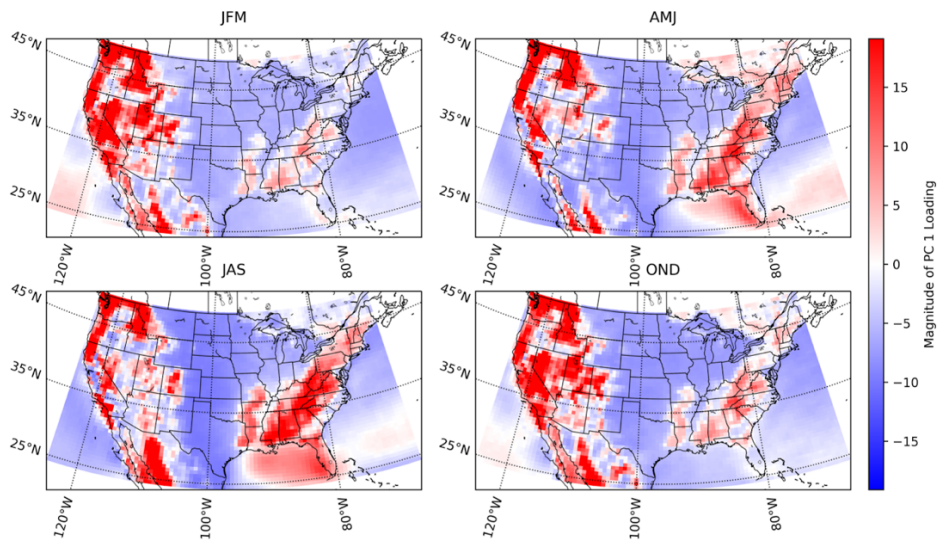


Figure 17. As in Figure 15 except for each season.

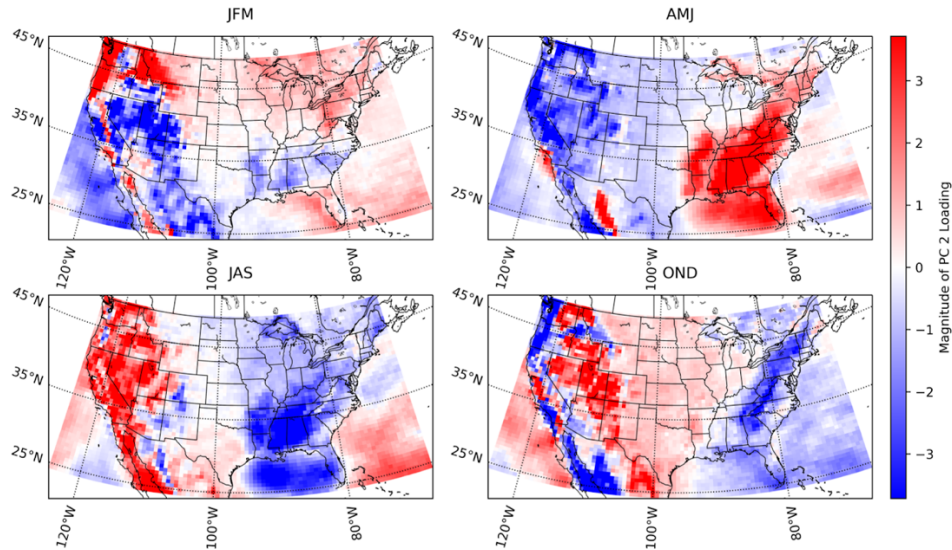


Figure 18. As in Figure 16 except for each season.

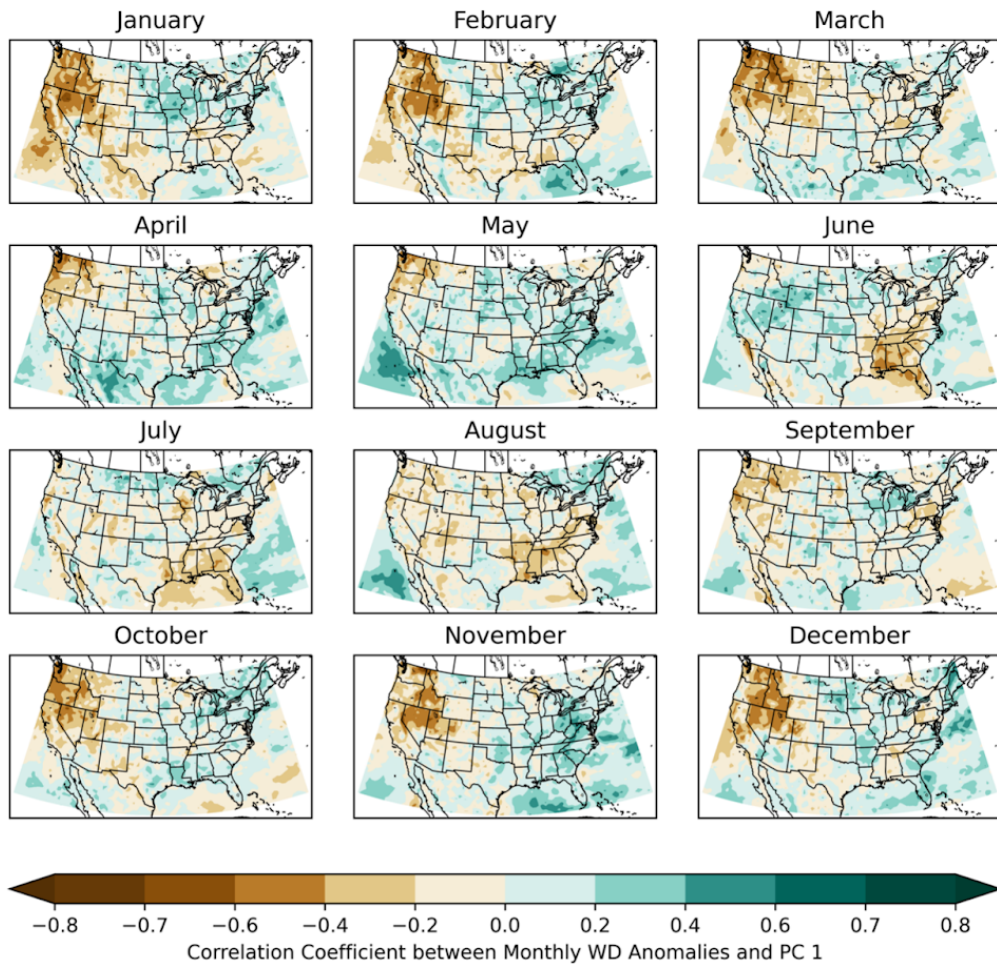


Figure 19. Monthly correlations between scaled WD Anomalies and PC time series for the first principal component. Loading signs have been flipped such that tan shading represents a positive correlation between the PC and the raw data while teal shading represents an inverse correlation.

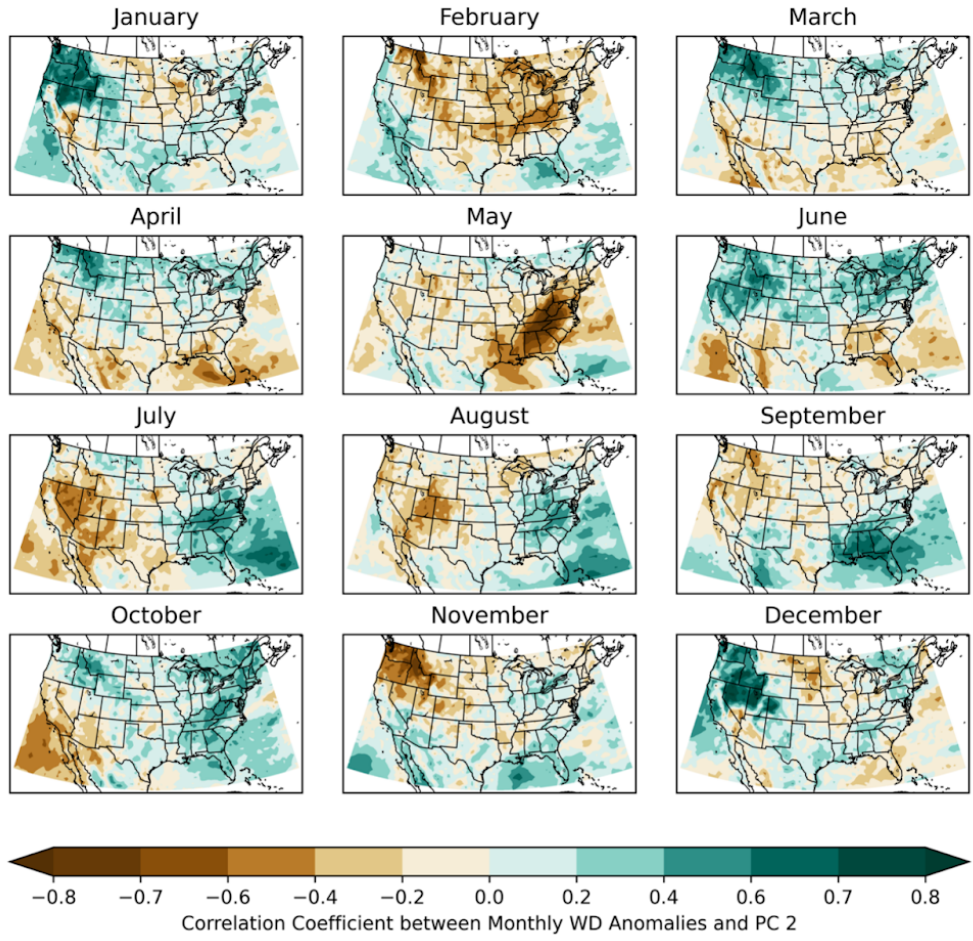


Figure 20. As in Figure 19 except for the second principal component.

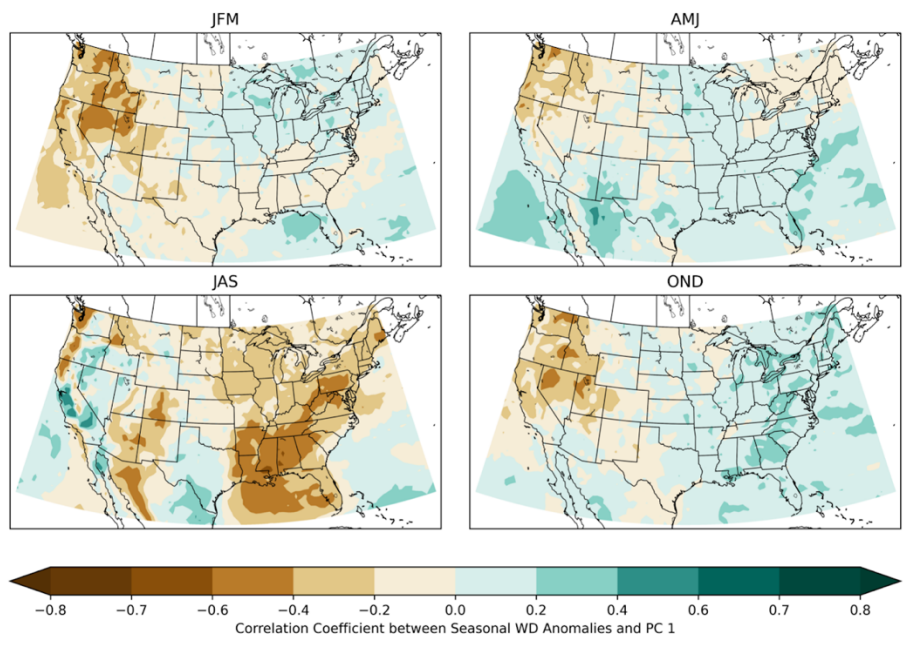


Figure 21. Correlation coefficient between seasonal WD Anomalies and WD Loadings for the first principal component.

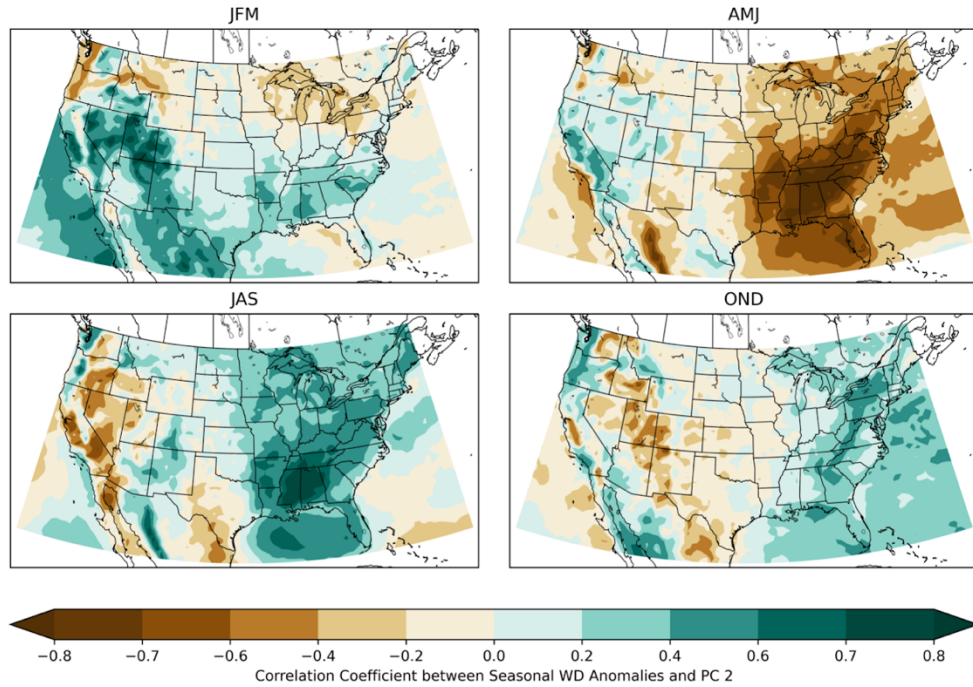


Figure 22. As in Figure 21 except for the second principal component.

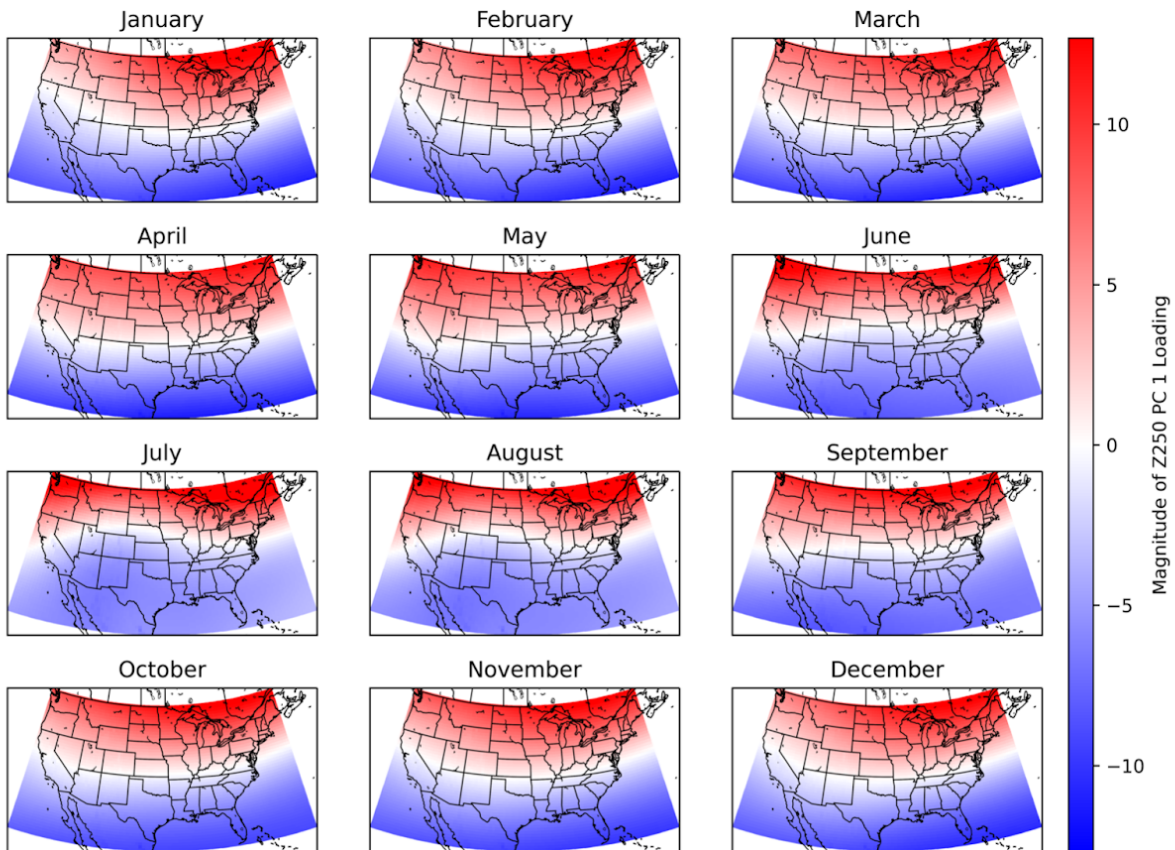


Figure 23. Spatial loadings of the first Principal Component of geopotential height at 250 hPa for each month. A climatological representation of the jet stream's monthly structure.

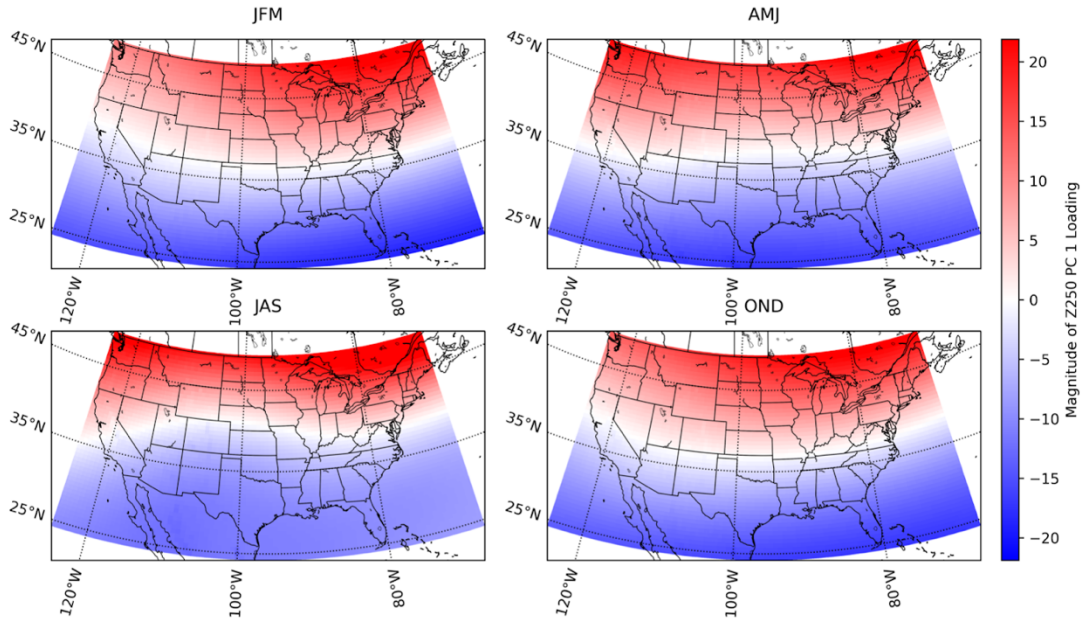


Figure 24. As in Figure 23 except for each season.

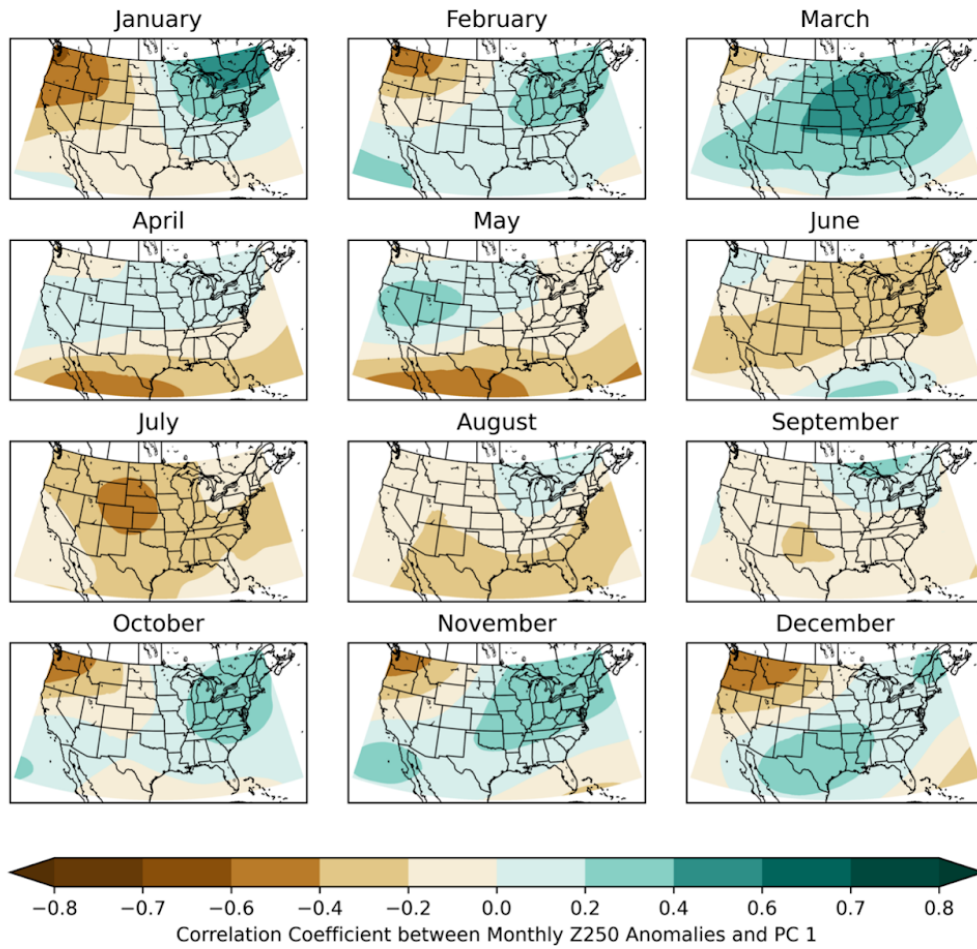


Figure 25. As in Figure 19 except for Z<sub>250</sub> anomalies.

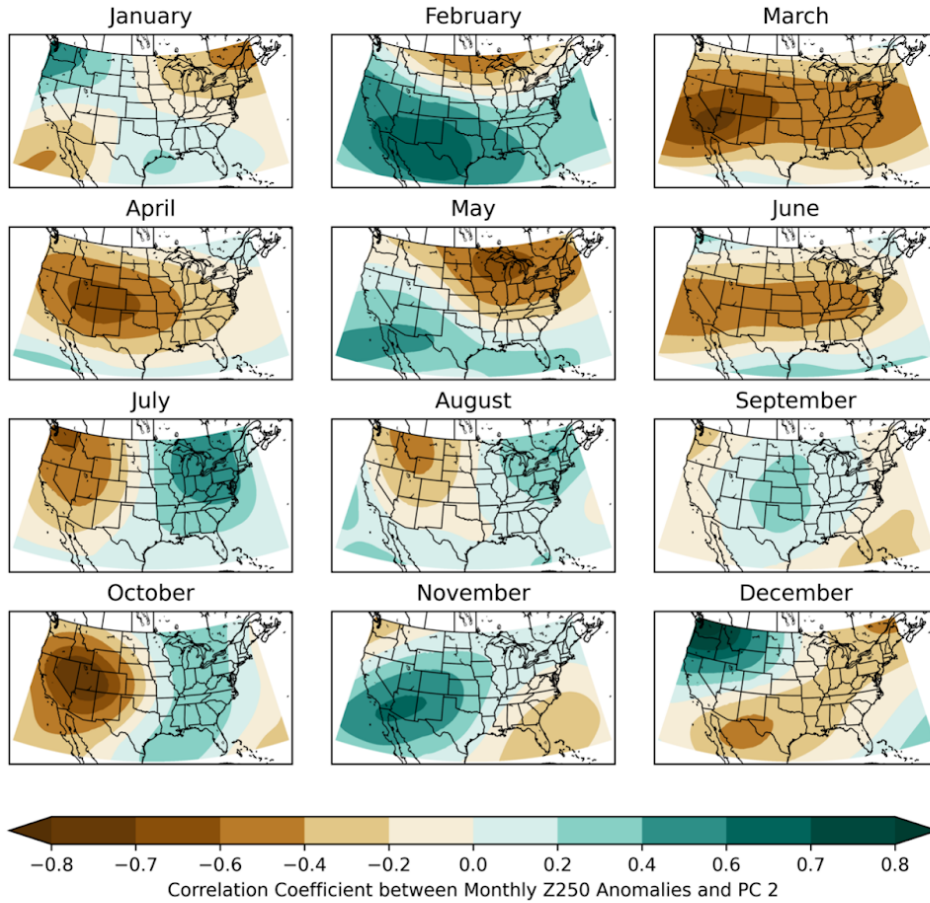


Figure 26. As in Figure 20 except for Z<sub>250</sub> Anomalies.

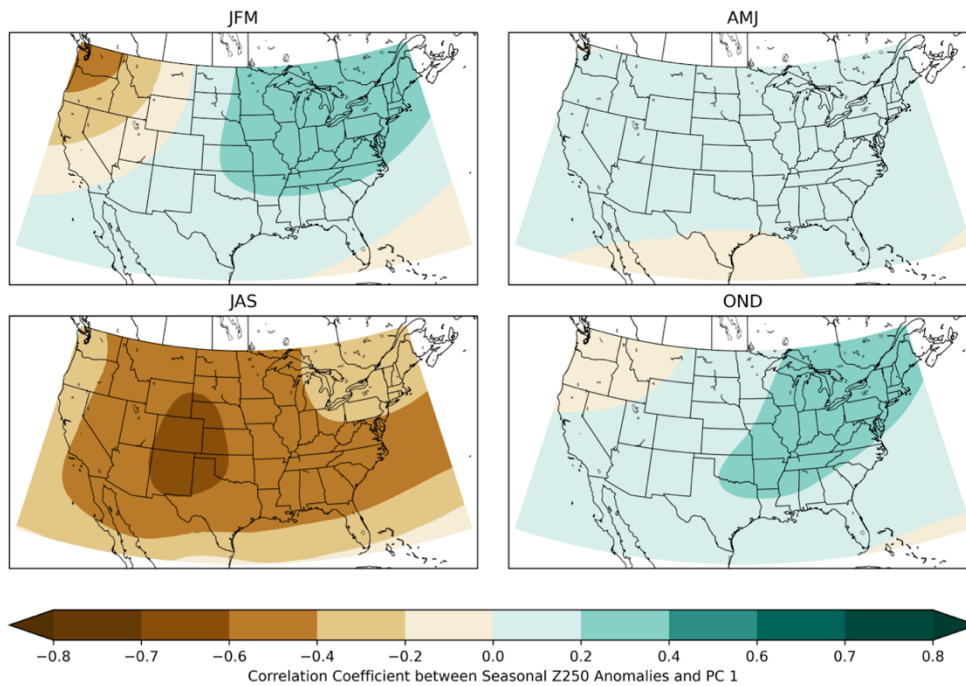


Figure 27. As in Figure 21 except for Z<sub>250</sub> anomalies.

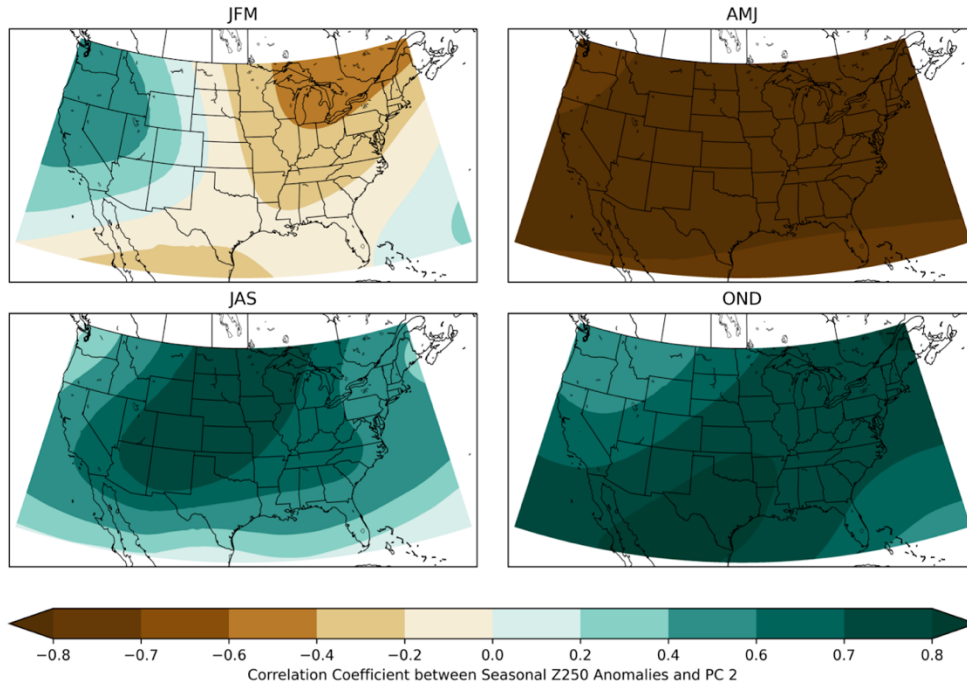


Figure 28. As in Figure 22 except for  $Z_{250}$  anomalies.

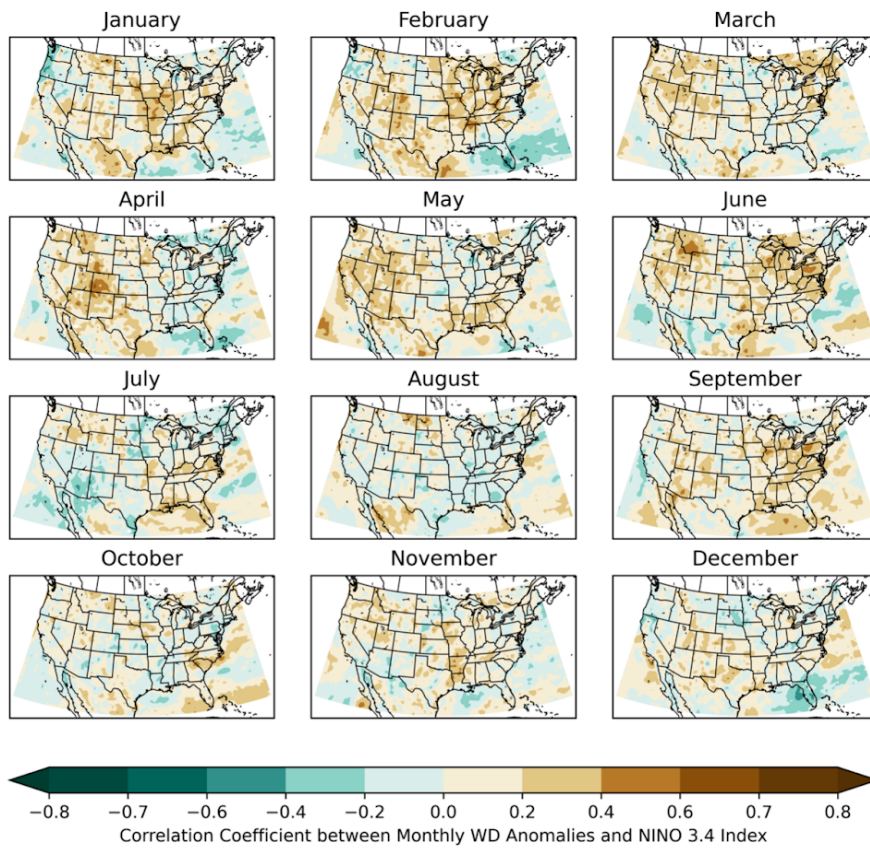


Figure 29. Monthly correlations between scaled WD Anomalies and SST anomalies over the NINO 3.4 region in the equatorial Pacific. Tan shading represents a positive correlation between the pattern index and WD Anomalies, while teal shading represents an inverse correlation.

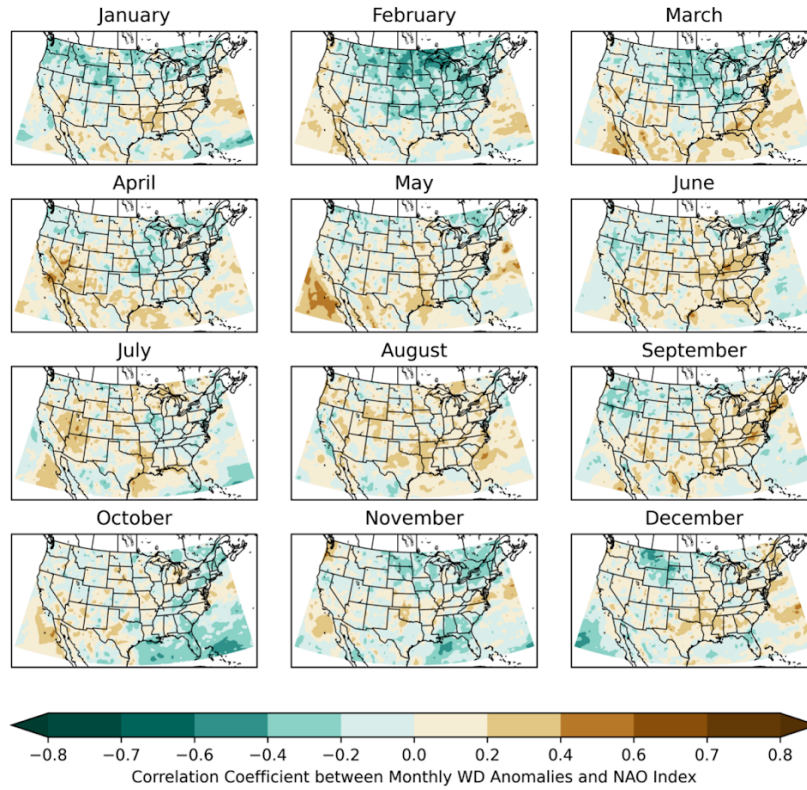


Figure 30. As in Figure 29 except for the North Atlantic Oscillation index.

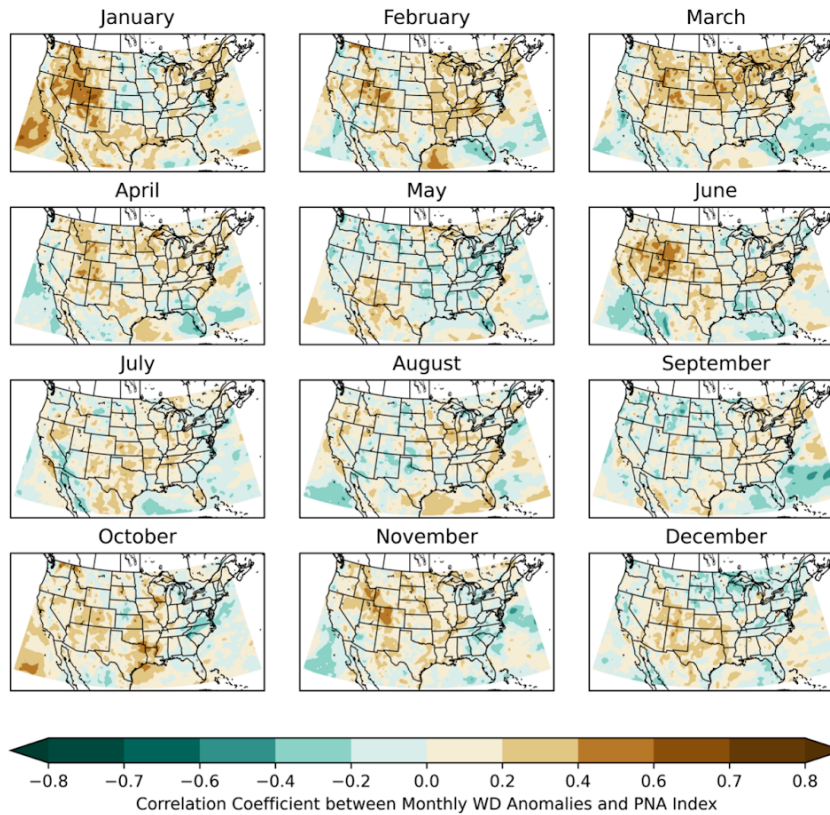


Figure 31. As in Figure 29 except for the Pacific/North American pattern index.

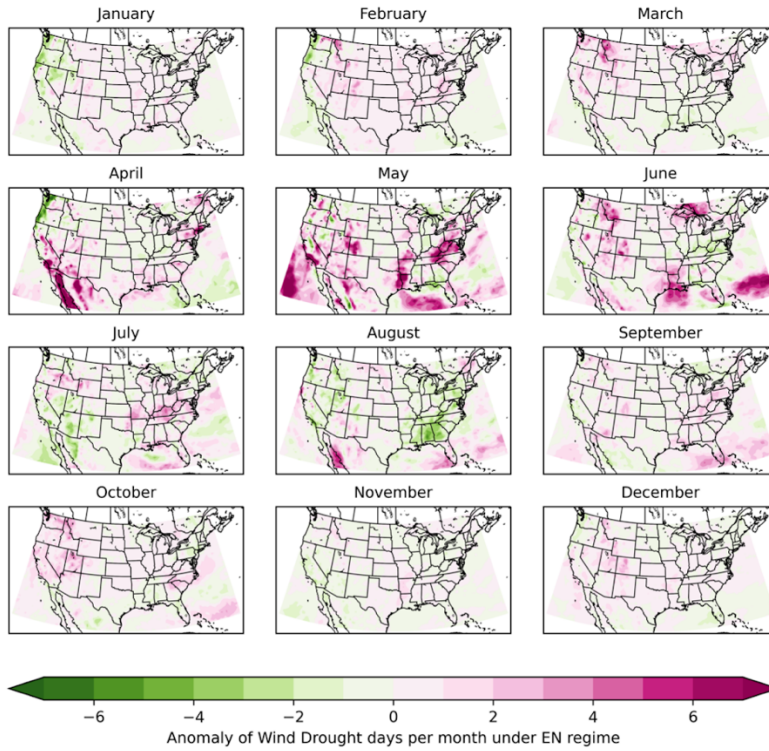


Figure 32. Composites of average monthly WD anomalies in months where the NINO 3.4 index exceeds 1.0 (El Niño). Purple shading represents a WD frequency for the months within the composite that exceeds the monthly WD average, while green shading represents a deficit in WD days for the composite compared to the monthly climatology.

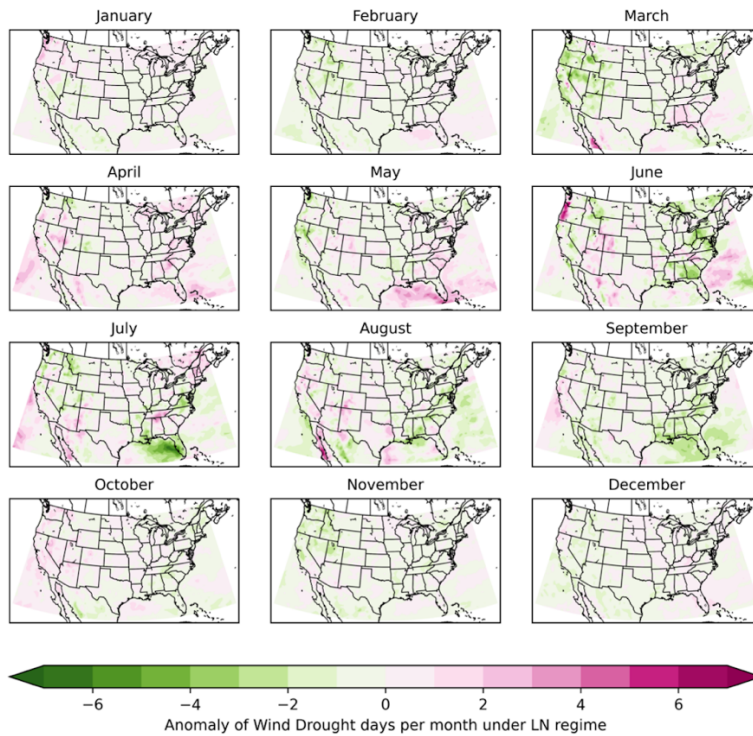


Figure 33. As in Figure 32 except for NINO 3.4 index below -1.0 (La Niña).

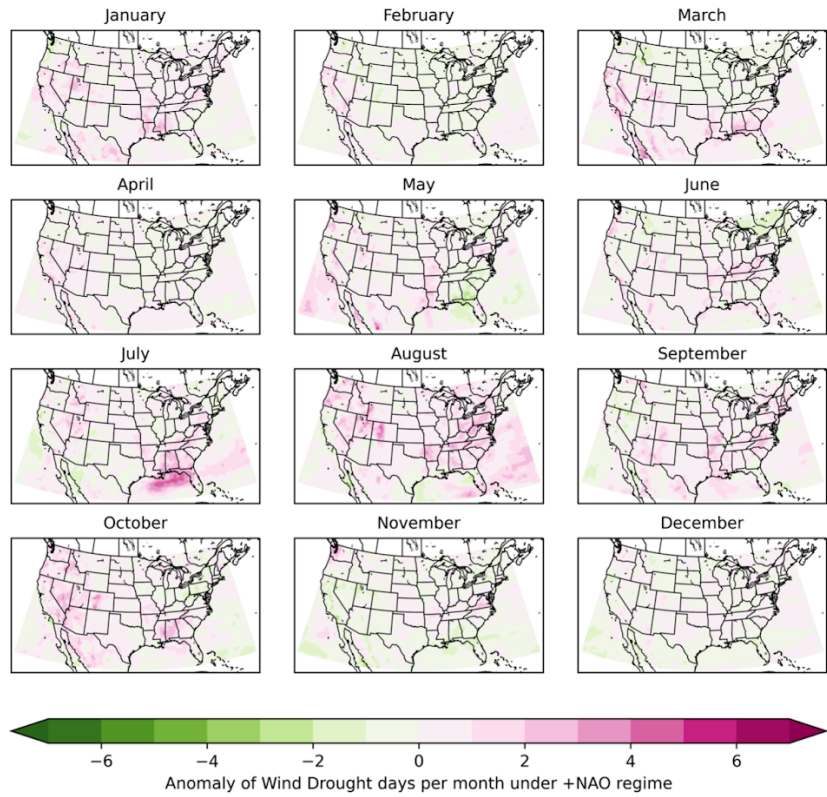


Figure 34. As in Figure 32 except for the positive phase of the NAO, where the index exceeds 1.0.

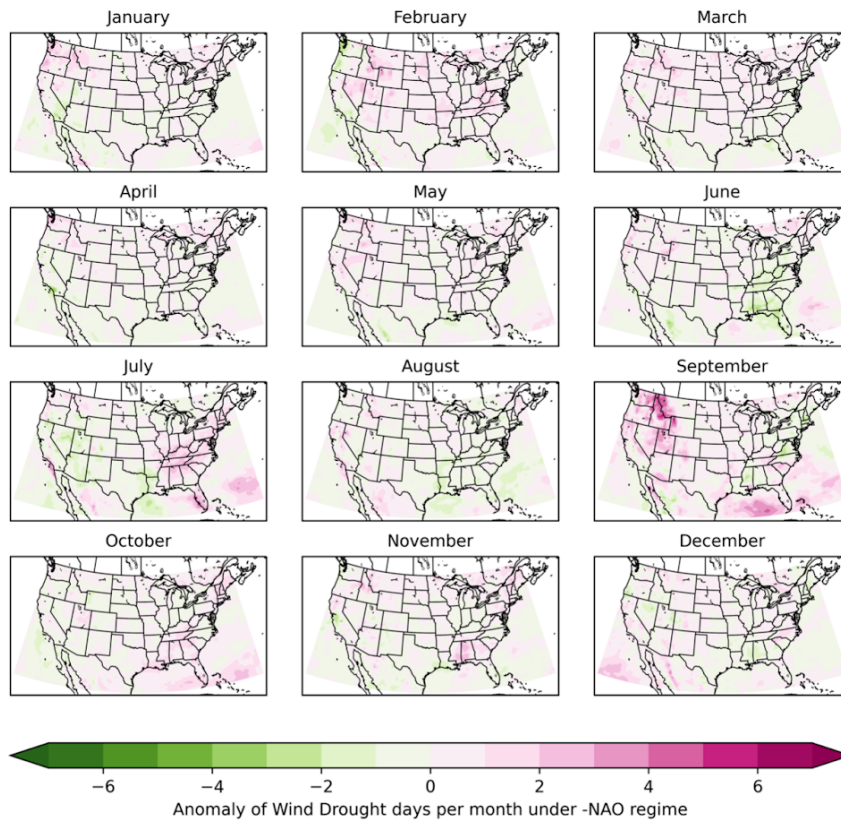


Figure 35. As in Figure 34 except for the negative phase of the NAO, when the index is less than -1.0.

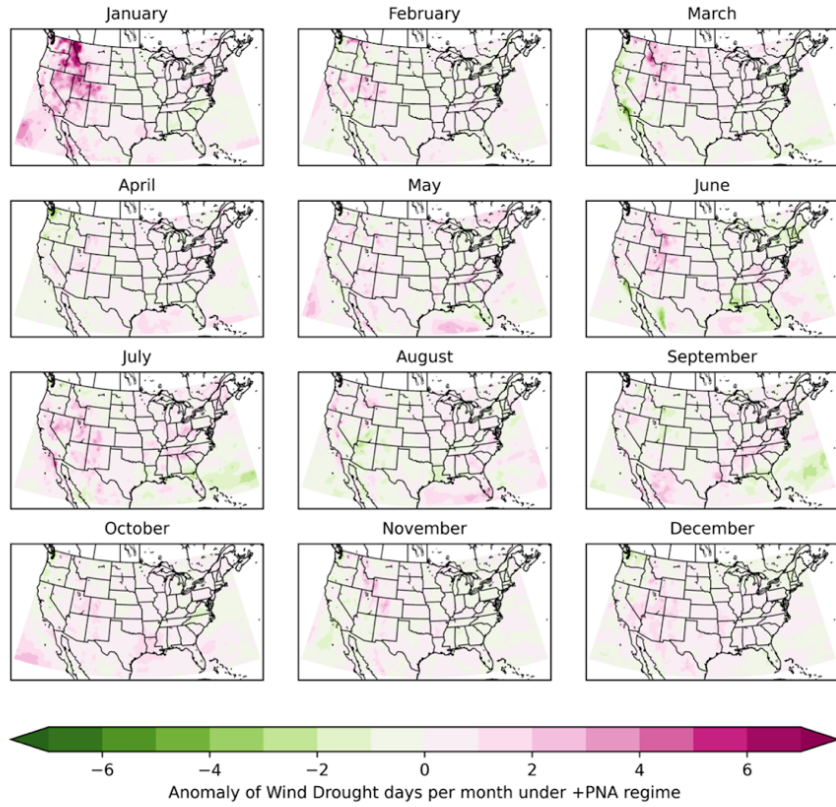


Figure 36. As in Figure 32 except for the positive phase of the PNA, where the index exceeds 1.0.

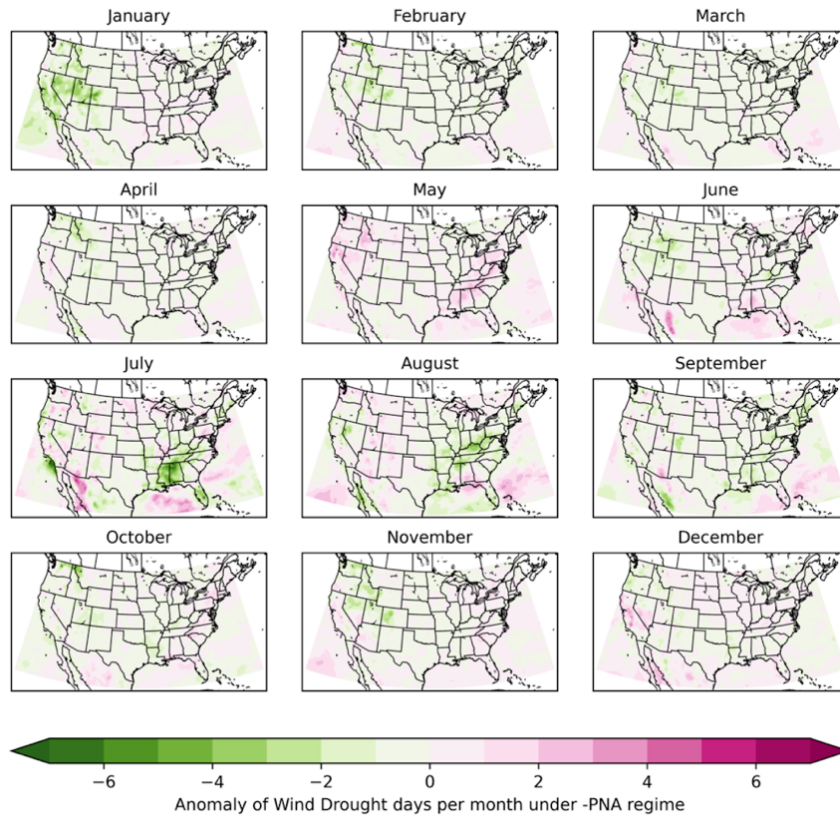


Figure 37. As in Figure 36 except for the negative phase of the PNA, where the index is less than -1.0.

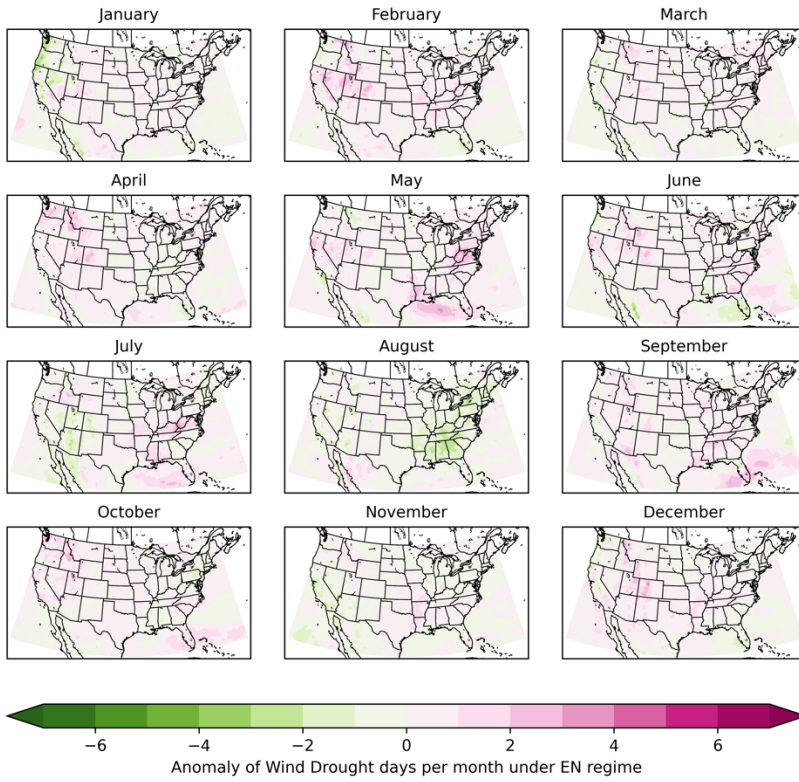


Figure 38. As in Figure 32 except for years (July-June) defined as a moderate to strong El Niño event.

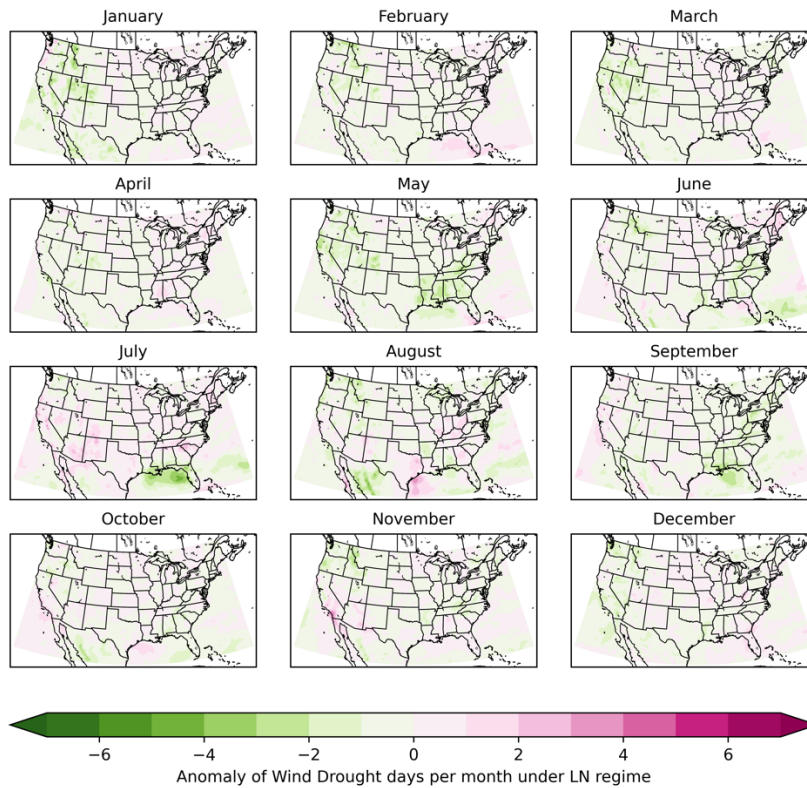


Figure 39. As in Figure 38 except for La Niña events.

## 7. REFERENCES

- Alder, W. J., Brough, R. C., Buchanan, S. T., James, D. R., Pope, D. W., & Tolman, B. T. (1996). *Daily Weather Almanac, 1847-1995*. Utah Center for Climate and Weather. <http://www.utahweather.org/2015/02/daily-weather-almanac-1847-1995.html>
- Armstrong, T. (2017, June). *Historic Heat Waves in the Carolinas*. NOAA's National Weather Service. <https://www.weather.gov/ilm/heatwaves>
- Bowen, T., Chernyakhovskiy, I., & Denholm, P. (2019). Grid-Scale Battery Storage: Frequently Asked Questions. *NREL Green Integration Toolkit*, 8.
- Global Modeling and Assimilation Office (GMAO) (2015), MERRA-2 instM\_3d\_ana\_Np: 3d,Monthly mean, Instantaneous, Pressure-Level, Analysis, Analyzed Meteorological Fields V5.12.4, Greenbelt, MD, USA, Goddard Earth Sciences Data and Information Services Center (GES DISC), Accessed: 23 April 2022, [10.5067/V92O8XZ30XBI](https://doi.org/10.5067/V92O8XZ30XBI)
- Gelaro, R., McCarty, W., Suárez, M. J., Todling, R., Molod, A., Takacs, L., Randles, C. A., Darmenov, A., Bosilovich, M. G., Reichle, R., Wargan, K., Coy, L., Cullather, R., Draper, C., Akella, S., Buchard, V., Conaty, A., Silva, A. M. da, Gu, W., ... Zhao, B. (2017). The Modern-Era Retrospective Analysis for Research and Applications, Version 2 (MERRA-2). *Journal of Climate*, 30(14), 5419–5454. <https://doi.org/10.1175/JCLI-D-16-0758.1>
- IEA (2021), *Global Energy Review 2021*. International Energy Agency, Paris <https://www.iea.org/reports/global-energy-review-2021>
- Mitchell, T. (2010, November). *Pacific/North American (PNA) Index*. North Atlantic Oscillation (NAO). [http://research.jisao.washington.edu/data\\_sets/pna/](http://research.jisao.washington.edu/data_sets/pna/)

- NCEP Climate Prediction Center. *CPC: SPECIAL CLIMATE SUMMARY 96/4: SUMMER 1996: Cool & Wet From the Great Plains Eastward—Hot And Dry in the West*. (1996, September). [https://www.cpc.ncep.noaa.gov/products/special\\_summaries/96\\_4/](https://www.cpc.ncep.noaa.gov/products/special_summaries/96_4/)
- NOAA National Centers for Environmental Information, State of the Climate: Monthly National Climate Report for August 2014, published online September 2014, retrieved on May 24, 2022 from <https://www.ncei.noaa.gov/access/monitoring/monthly-report/national/201408>.
- NOAA National Centers for Environmental information, Climate at a Glance: Statewide Time Series, published online May 2022, <https://www.ncdc.noaa.gov/cag/>
- NOAA National Centers for Environmental Information, State of the Climate: Monthly National Climate Report for August 2005, published online September 2005, <https://www.ncei.noaa.gov/access/monitoring/monthly-report/national/200508>.
- Null, J. (2022, April). *El Niño and La Niña Years and Intensities*. Golden Gate Weather Services. <https://ggweather.com/enso/oni.htm>
- Osborn, T. J. (2010, October). *North Atlantic Oscillation (NAO)*. <https://crudata.uea.ac.uk/cru/data/nao/viz.htm>
- Pryor, S. C., Shepherd, T. J., & Barthelmie, R. J. (2018). Interannual variability of wind climates and wind turbine annual energy production. *Wind Energy Science*, 3(2), 651–665. <https://doi.org/10.5194/wes-3-651-2018>
- Pryor, S. C., Letson, F. W., & Barthelmie, R. J. (2020). Variability in Wind Energy Generation across the Contiguous United States. *Journal of Applied Meteorology and Climatology*, 59(12), 2021–2039. <https://doi.org/10.1175/JAMC-D-20-0162.1>

- Ropelewski, C. F., Lamb, P. J., & Portis, D. H. (1993). The Global Climate for June to August 1990: Drought Returns to Sub-Saharan West Africa and Warm Southern Oscillation Episode Conditions Develop in the Central Pacific. *Journal of Climate*, 6(11), 2188–2212. [https://doi.org/10.1175/1520-0442\(1993\)006<2188:TGCFJT>2.0.CO;2](https://doi.org/10.1175/1520-0442(1993)006<2188:TGCFJT>2.0.CO;2)
- Stull, R. B. (1988). Mean Boundary Layer Characteristics. In R. B. Stull (Ed.), *An Introduction to Boundary Layer Meteorology* (pp. 1–27). Springer Netherlands. [https://doi.org/10.1007/978-94-009-3027-8\\_1](https://doi.org/10.1007/978-94-009-3027-8_1)
- Wamstead, D., Feaster, S., & Schlissel, D. (2022). *U.S. 2022 Power Sector Outlook*. Institute for Energy Economics and Financial Analysis. [https://ieefa.org/wp-content/uploads/2022/04/2022-US-Power-Sector-Outlook\\_April-2022.pdf](https://ieefa.org/wp-content/uploads/2022/04/2022-US-Power-Sector-Outlook_April-2022.pdf)
- Yu, Z.; Tuzuner, A. Fractional weibull wind speed modeling for wind power production estimation. Power & Energy Society General Meeting, 2009. PES'09. IEEE. 2009; p 4.